

# Deformation regimes and the rheological evolution of fault zones in the lithosphere: the effects of pressure, temperature, grainsize and time

MARK R. HANDY

*Geologisches Institut, Universität Bern, Baltzerstrasse 1, 3012 Bern (Switzerland)*

(Received November 16, 1987; revised version accepted September 26, 1988)

## Abstract

Handy, M.R., 1989. Deformation regimes and the rheological evolution of fault zones in the lithosphere: the effects of pressure, temperature, grainsize and time. *Tectonophysics*, 163: 119–152.

A new series of two- and three-dimensional deformation regime maps facilitating the simultaneous display of petrological, microstructural, and rock-mechanical information illustrates the pressure, temperature and grainsize dependencies of brittle, crystal-plastic and granular creep regimes in the lithosphere. The predictions made using the extrapolated laboratory data are in qualitative agreement with inferences drawn from microstructural studies in naturally deformed monomineralic rocks. The deformation regime maps are used to show that the rheological evolution of a fault zone is related both to its location within a compositionally heterogeneous lithospheric section and to the pressure–temperature–time history of that section. Strain localization into ductile shear zones is accelerated if grainsize reduction leads to a change from grainsize-insensitive to grainsize-sensitive creep. In rocks whose rheology is approximated by the flow of one weak mineral, this process is favored at high stress–low temperature, and/or retrograde thermal conditions. For polymineralic rocks in either prograde or retrograde thermal settings, reaction-induced or -enhanced switches to grainsize-sensitive creep can occur at depths corresponding to the intersection of the ambient geothermal gradient or pressure–temperature–time path with the limits of mineral stabilities for a specified rock composition. The consideration of the effects of pressure, temperature, grainsize and syntectonic reactions on fault rheology results in an evolutionary rheological model of an extending lithosphere which is more complex than existing models.

## 1. Introduction

An increasing number of geological, geophysical and geodetic observations suggests that large-scale strain of the continental lithosphere is accommodated within networks of relatively narrow shear zones (Ramsey, 1980; Zobach et al., 1985). Ostensibly, the development of such zones is due to the localization of strain via several deformation mechanisms (e.g., cataclasis, dynamic recovery and recrystallization and diffusion-accommodated grain-boundary sliding) which can cause a localized decrease in viscosity with respect

to the surrounding rock. The varying dependencies of these mechanisms on the physical conditions of the deformation affect the dynamics and kinematics of the deformation and determine the structure of the lithosphere. In particular, the interaction of pressure- and temperature-sensitive metamorphic and deformational processes influences significantly the rheological evolution of major shear zones.

This paper examines the influence of strain rate, stress, grainsize, pressure and temperature on the relative activities of brittle, crystal-plastic and granular creep regimes in the lithosphere. Mechan-

ical equilibrium diagrams (deformation regime diagrams) are introduced which enable the direct comparison of experimental rock deformation data with mechanical inferences from microstructural studies of naturally deformed rocks. Section 2 reviews the fracture and creep data in the literature that are used to construct the deformation regime diagrams in this paper. Creep laws for hydrous polycrystalline olivine are extracted from a common set of steady-state creep data in the literature. Section 3 considers the effects of pressure, temperature and grain size on the stability fields of the deformation regimes. In Section 4, the deformation regime diagrams are used to show various generic rheological histories undergone by shear zones in the lithosphere. Finally, the rheological trajectories of fault zones presented in the previous sections are incorporated into an evolutionary rheological model of the continental crust and uppermost mantle.

## 2. The construction of deformation regime maps

### 2.1. General

The concept of a mechanical equilibrium diagram was introduced by Donath et al. (1971) as a convenient means of showing how various styles or "modes" of deformation observed in experimentally deformed rocks are related to the experimentally imposed environmental conditions. While their "deformation mode field" diagrams focussed on the effects of confining pressure and strain, Donath and his coworkers also recognized the importance of strain rate, rock composition and structural anisotropy to the deformational behavior of rocks (Donath, 1964; Donath and Fruth, 1971). Ashby (1972) combined theoretical constitutive equations with experimental data for metals to construct "deformation mechanism maps", an approach already employed in simpler form by Weertman (1968). Stocker and Ashby (1973), Ashby and Verrall (1978), and Carter and Tsenn (1987) then used the maps to show how deformation mechanisms are related to important geophysical parameters such as stress, strain rate, pressure, temperature and grain size. These dependencies are commonly expressed in the form of

constitutive equations, or flow laws. The boundaries between two mechanism fields on a deformation mechanism map correspond to the conditions at which those two mechanisms are in mechanical equilibrium. Since the flow laws used for the maps in this paper are experimentally rather than theoretically derived, the diagrams and maps are referred to as *deformation regime maps*, following the usage of Schmid et al. (1977) and Paterson (1987). Transient creep is not included in the maps due to the paucity of relevant data for rocks as well as to the comparatively small times and strains over which such behavior is thought to predominate (see Carter and Kirby, 1978).

To illustrate the geological discussion in the following sections, two different coordinate systems are used: shear strain-rate-temperature-pressure ( $\log \dot{\gamma}$ - $T$ - $P$  diagrams in Section 3) and strain rate-temperature-grain size ( $\log \dot{\gamma}$ - $T$ - $\log d$  diagrams in Section 4). Both coordinate systems depict grain size-insensitive (GSI) and grain size-sensitive (GSS) creep regimes. Shear strain rate is chosen as the independent deformational variable instead of the differential shear stress for two basic reasons: (1) elasto-viscous deformational processes are implicitly rate- (i.e. time-) dependent. Time and, particularly, strain are better constrained by direct geological observation than is stress; (2) geological and geophysical problems often entail kinematic boundary conditions such as displacement rate or plate velocity. The equations used to define the equilibrium boundary curves between deformation regimes in these coordinates are derived in the Appendix and are based on the flow laws described below.

The deformation regime maps in the next two sections of this paper are constructed for polycrystalline olivine and cover pressure and temperature conditions typical of the continental crust and uppermost mantle. Olivine exists stably in the upper mantle to depths of about 400 km, below which it breaks down to spinel. It is unstable or exists only metastably in the sialic crust at depths generally less than 60 km (for thickened continental crust with a low geothermal gradient) or 10 to 20 km (for oceanic crust or thinned continental crust with a high geothermal gradient). Although the rheological behavior of olivine pertains more

to the upper mantle, the general form of the creep equations is the same as for other important rock-forming minerals. In this instance, the choice of polycrystalline olivine was dictated by the greater quality and quantity of published experimental data and also by the fact that grainsize effects in olivine are currently better constrained than in quartz or feldspar. Keeping in mind the admonitions of Paterson (1987) regarding the extrapolation of laboratory data to geological conditions, I emphasize that the deformation regime maps are interpreted semi-quantitatively. Poor constraints on the position of the equilibrium curves betray the yet incomplete knowledge of the effects of grainsize, pressure, structural anisotropy, strain and chemical environment on the creep behavior of rocks. Despite this caveat, the similarity of microstructures in deformed rocks of widely varying composition indicates that the general position of the mechanical equilibrium curves shown here for polycrystalline olivine may serve as a guide to the deformational behavior of other lithologies.

## 2.2. Viscous creep laws

The steady-state creep laws employed in the construction of the diagrams are:

$$\dot{\gamma} = \sqrt{3}^{n+1} A \exp\left(\frac{-Q}{RT}\right) \tau^n d^{-m} \quad (1)$$

for power law creep and:

$$\dot{\gamma} = \sqrt{3} B \exp\left(\frac{-Q}{RT}\right) \exp(\sqrt{3} C \tau) \quad (2)$$

for exponential law creep, where  $\dot{\gamma}$  is the shear strain rate ( $\text{s}^{-1}$ );  $A$  and  $B$  are pre-exponential structure-factors;  $Q$  is the apparent activation energy of creep;  $R$  is the gas constant;  $T$  is the absolute temperature;  $n$  is the dimensionless stress exponent;  $m$  is the dimensionless grainsize exponent;  $C$  is the stress function;  $\tau$  is the shear stress;  $d$  is the grainsize.

$A$ ,  $B$ ,  $C$ ,  $Q$ ,  $n$  and  $m$  are all material parameters which can be derived from a multilinear regression analysis of creep data (e.g. Fig. 1).  $\sqrt{3}$  is the factor converting the axi-symmetric stresses and strain rates of laboratory flow laws ( $\sigma$  and  $\dot{\epsilon}$  in eqns. 3 and 4) into octahedral or simple shear

stresses and strain rates more closely approximating natural shear conditions (Nye, 1953):

$$\tau = \frac{1}{\sqrt{3}} \sigma \quad (3)$$

$$\dot{\gamma} = \sqrt{3} \dot{\epsilon} \quad (4)$$

The material constants for polycrystalline olivine listed in Table 1 were extracted from the experiments on "wet" dunite of Chopra and Paterson (1981) and on sintered dunite aggregates of Karato et al. (1986). The dominant deformation mechanisms inferred from the authors' microstructural studies of the deformed specimens are also listed. The exponential law creep and grain-size-insensitive (GSI) power law creep parameters in Table 1 are derived from a best fit of the Chopra and Paterson (1981) steady-state creep data for Anita Bay dunite (average grainsize = 100  $\mu\text{m}$ ) to a hyperbolic sine creep function (Fig. 1a) of the form (Garofolo, 1965):

$$\dot{\gamma} = \sqrt{3} D \exp\left(\frac{-Q}{RT}\right) \left[ \sinh\left(\frac{\sqrt{3} \tau}{\alpha}\right) \right]^n \quad (5)$$

where  $A = D/2^n$ ,  $B = D/\alpha^n$  and  $C = n/\alpha$  in eqns. (1) and (2) and the other parameters are defined above. Only those data (17 points) were included in Fig. 1 which the authors indicate had attained mechanical steady-state (Chopra and Paterson, 1981; their table II).

The creep data plotted in Fig. 1 were normalized to a reference temperature,  $T_{\text{ref}}$ , of 1000 °C with the relation:

$$\log \dot{\epsilon}_{\text{nor}} = \log \dot{\epsilon}_{\text{ex}} + \frac{Q}{R \ln 10} \left( \frac{1}{T_{\text{ex}}} - \frac{1}{T_{\text{ref}}} \right) \quad (6)$$

where  $\dot{\epsilon}_{\text{nor}}$  = the normalized strain rate at  $T_{\text{ref}}$  and  $\dot{\epsilon}_{\text{ex}}$  = the experimental strain rate at  $T_{\text{ex}}$ , the experimental temperature.

An activation energy,  $Q$ , of 444 kJ/mole was used to normalize the experimental strain rates to 1000 °C. For Anita Bay dunite, this activation energy probably has greatest validity at stresses above 100 MPa, since stress-relaxation tests indicate lower values of  $n$  (2.44) and  $Q$  (386 kJ/mole) at stresses less than 100 MPa (Chopra and Paterson, 1981). The authors attribute this to the weakening effect of water at the grain boundaries,

TABLE 1

Viscous creep parameters for hydrous polycrystalline olivine (dunite)

Creep regime	Log <i>A</i>	Log <i>B</i>	Log <i>D</i>	<i>Q</i>	<i>n</i>	<i>C</i>	$\alpha$	<i>m</i>	Inferred deformation mechanism	Remarks
Hyperbolic sine law			15.48	444 ± 24	3.67		1965	0	dislocation glide and dislocation creep	best fit of steady-state creep tests on Anita Bay dunite of Chopra and Paterson (1981) to eqn. (5)
Exponential law		14.38		444 ± 24		1.87 × 10 <sup>-3</sup>		0	dislocation glide + incipient dislocation creep	best fit of steady-state creep tests on Anita Bay dunite to eqn. (2)
GSI-power law	3.41			444 ± 24	3.67			0	dislocation creep	best fit of steady-state creep tests on Anita Bay dunite to eqn. (1)
GSS-power law	8.47			356 ± 121 *	1.4 ± 0.3			2.5	diffusion-accommodated	creep tests in gas medium
GSS-power law	6.53			297 **	1.4 ± 0.3			2.5	grain-boundary sliding (assume equal contributions of grain-boundary and volume accommodation of sliding)	<i>P</i> = 300 MPa, <i>T</i> = 1000–1300 °C $\dot{\epsilon}$ = 10 <sup>-3</sup> – 10 <sup>-6</sup> s <sup>-1</sup> based on data of Karato et al. (1986); sintered aggregates of Anita Bay dunite (see text)

Units: *A* in MPa<sup>-*n*</sup> s<sup>-1</sup>, *Q* in kJ/mole, *C* in MPa<sup>-1</sup>,  $\alpha$  in MPa, *B* and *D* in s<sup>-1</sup>.

Errors: ±1 (95%) confidence limits, as reported in the sources above.

\* Activation energy of grain-size-sensitive (GSS) creep taken from hot-pressing experiments of Schwenn and Goetze (1978).

\*\* Activation energy of GSS creep estimated as 0.67 of the activation energy of grain-size-insensitive (GSI) creep (see text).

an effect which is more pronounced for finer grain-sizes.

Post (1977) has shown that eqn. (5) is valid for polycrystalline olivine over the range of high and low differential stresses covered by eqns. (1) and (2), respectively. Figures 1a, b and c compare the fit of Chopra and Paterson's data to eqns. (5), (2) and (1). Over the entire stress range of the experiments, the correlation coefficient of the hyperbolic sine law fit (Fig. 1a;  $r = -0.981$ ) is the same as that of the optimum power law fit (Fig. 1b) and much better than that of the exponential law fit (Fig. 1c). Figure 1c shows that for stresses greater than ca. 200 MPa, the stress sensitivity of Anita Bay dunite increases markedly. For the nine ex-

perimental points above this threshold stress, the data are only slightly better fit by the power law ( $r = -0.953$ ) than by the exponential law ( $r = -0.948$ ). The coarser grained Aheim dunite (ave. grain-size = 900  $\mu\text{m}$ ) exhibits the same behavior, but the transitional stress to greater stress sensitivity is a bit higher, at ca. 250 MPa (Fig. 1c). The best fit to the hyperbolic sine law yields *n*-values of 3.67 and 4.54, respectively, for Anita Bay and Aheim dunites. These values are somewhat higher than the *n*-values of 3.35 and 4.48 quoted by Chopra and Paterson (1981; their table IV) for a power law fit of the steady-state creep data above stresses of 100 MPa. The aim of this re-analysis was to compare the relative activity of exponential

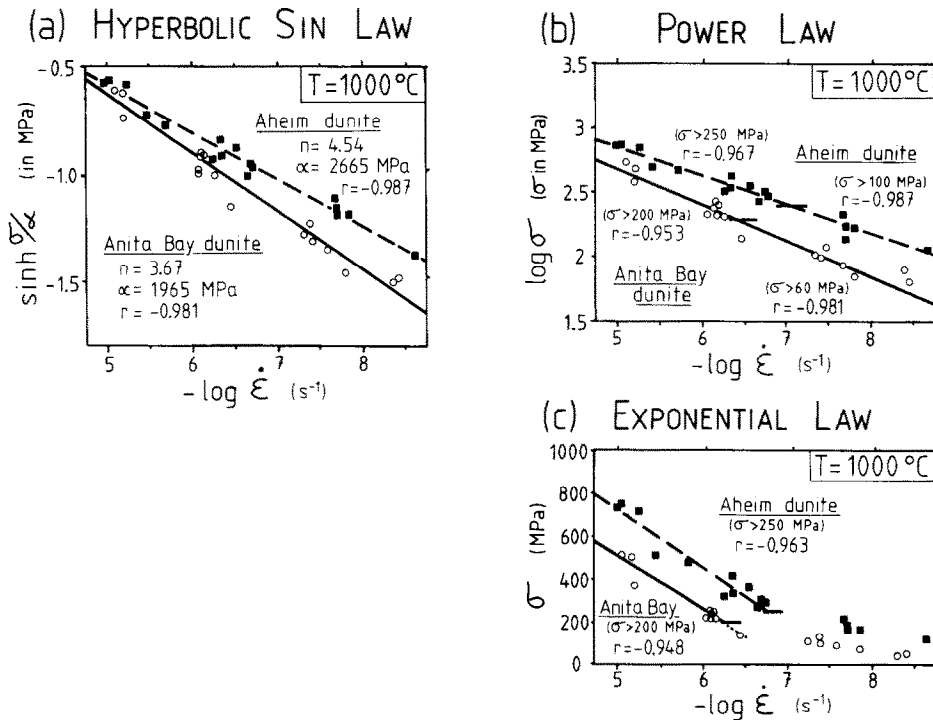


Fig. 1. Fit of the steady state creep-data of Chopra and Paterson (1981, their table II) to three different creep functions (eqns. 1, 2 and 5 in the text). The data is normalized to  $1000^\circ\text{C}$  using  $Q = 444$  kJ/mole for Anita Bay dunite (solid line, open circles) and  $498$  kJ/mole for Aheim dunite (dashed line, solid squares). Only those runs which the authors indicate have achieved mechanical steady state are included in the fit.

- Fit of data to hyperbolic sine function (eqn. 5). Compare the correlation coefficients with those in (b) and (c). Recall that an ideal fit of the data to a straight line with a negative slope is  $r = -1$ .
- Fit of the data to a power function (eqn. 1). Symbols as in (a).
- Fit of the data to an exponential function (eqn. 2). The best fits in this figure are for  $\sigma > 200$  MPa (Anita Bay dunite) and  $\sigma > 250$  MPa (Aheim dunite). Compare these correlation coefficients with those in (b) for the same stress range.

and power law creep (Section 3) based on a common, internally consistent set of data. The steady-state creep data of Chopra and Paterson (1981) and Karato et al. (1986) were used in this study because the reported sensitivity of stress measurements in their experiments ( $< 1$  MPa; gas-medium apparatus with an internal load cell) is much better than in previous creep tests of olivine (where ascertainable).

Grainsize-sensitive creep laws for polycrystalline olivine (Table 1) were derived from the creep data and observations of Karato et al. (1986) after the procedure of Paterson (1987). In the creep experiments, the transition in deformation regimes from grainsize-insensitive (GSI) to grainsize-sensitive (GSS) power law creep occurs at a grainsize of  $50 \mu\text{m}$  and a differential stress of about  $70$  MPa at a temperature of  $1300^\circ\text{C}$  and a strain rate of  $10^{-5}$

s $^{-1}$ . Together with a value for the activation energy of GSS creep, these data permit the calculation of the pre-exponential factor,  $A$ , in eqn. (1) above. Two different GSS flow laws for dunite are listed in Table 1. The first one is constructed for an activation energy of  $356$  kJ/mole, the value obtained by Schwenn and Goetze (1978) from porous olivine aggregates that displayed grainsize sensitivity of strain rate during hot pressing. The second creep law contains an assumed activation energy of  $297$  kJ/mole for GSS creep which is two thirds of the activation energy of GSI creep ( $Q = 444$  kJ/mole; Chopra and Paterson, 1981). A ratio of ca.  $0.5$  to  $0.67$  in the GSS- and GSI-activation energies has been observed in other materials (e.g. Solenhofen limestone; Schmid et al., 1977) and corresponds roughly with the ratio of the activation energy of grain-boundary diffusion to volume

self-diffusion of the rate-limiting species in the crystal lattice. An average value of 2.5 for the grainsize exponent is assumed, since Karato et al. (1986) found values of  $m$  ranging from 1.7 (dry conditions) to 3.4 (wet conditions). The effects of varying  $m$  are discussed in Section 3.1 (Fig. 4).

### 2.3. Brittle failure and frictional sliding

The deformation regime diagrams include an equilibrium field for brittle failure and frictional sliding based on the Mohr-Coulomb criterion:

$$\tau = \tau_0 + \mu \sigma_n \quad (7)$$

where  $\tau_0$  is the critical shear stress,  $\sigma_n$  is the normal stress on the sliding surface,  $\mu$  is the coefficient of maximum friction and  $\tau$  is the maximum shear stress on the sliding surface. This equation may be recast as (Sibson, 1977):

$$\tau = \frac{1}{2} [a + \sigma_3(b - 1)] \quad (8)$$

where  $a = 2\tau_0\sqrt{b}$ ,  $b = (\sqrt{1 - \mu^2} - \mu)^{-2}$  and  $\sigma_3 = P_e$ , the effective confining pressure.

Setting the least compressive principal stress,  $\sigma_3$ , equal to the effective confining pressure conforms with the triaxial stress state in experimental deformation apparatuses ( $\sigma_1 > \sigma_2 = \sigma_3$ ) and is a

convenient approximation of more general stress states in nature ( $\sigma_1 \geq \sigma_2 \geq \sigma_3$ ). The factor  $1/2$  replaces the octahedral shear factor,  $1/\sqrt{3}$ , in eqn. (3), since cataclasis during frictional sliding involves dilation and violates the condition of incompressible flow implicit in eqns. (3) and (4). The effective pressure,  $P_e$  (here defined in the sense of Terzaghi), is:

$$P_e = P(1 - \lambda) \quad (9)$$

where  $P$  is the total or lithostatic pressure and  $\lambda = P_{\text{pore}}/P$ .

The Mohr-Coulomb criterion provides a useful approximation of brittle behavior in the lithosphere, particularly at effective pressures above ca. 100 MPa, where the initial surface roughness of faults has little or no effect on friction (Mogi, 1974; Byerlee, 1978). Different values of the frictional constants  $\tau_0$ ,  $\mu$ ,  $a$ , and  $b$  employed in eqns. (7) and (8) are listed from the rock-mechanical literature in Table 2. These show that the frictional strength of rocks is generally independent of lithology, temperature and pressure for  $P_e < 800$ –1500 MPa and  $T < 400$ –600 °C (Stesky, 1978). Above these pressures and temperatures, the frictional coefficient,  $\mu$ , decreases and the critical shear strength,  $\tau_0$ , of rocks increases to an extent dependent on lithology. Generally, devia-

TABLE 2

Experimental frictional parameters of some crystalline rocks \*

$\mu$	$\tau_0$ (MPa)	$a$ (MPa)	$b$	$T$ (°C)	$\sigma_n$ (MPa)	Sources **	Rock type
0.85	0	0	4.68	25	< 200	(1)	wide range of lithologies; only
0.6	50	180	3.1	25	200–1700	(1)	10–15% variation in frictional strength with lithology
0.6	70–80	250–280	3.1	25–400	250–600	(2)	San Marcos Gabbro, Westerly Granite
0.6	20	70	3.1	500–600	250–600	(2)	San Marcos Gabbro <sup>a</sup>
0.3	170	470	1.8	500–600	> 600	(2)	San Marcos Gabbro
0.45	0	0	2.39	700	250–600	(2)	San Marcos Gabbro <sup>b</sup>
0.2	200	500	1.6	700	> 600	(2)	San Marcos Gabbro <sup>b</sup>
0.3–0.4	–	–	1.8–2.2	600–1000	500–1500	(3)	Hale Albite Rock <sup>c</sup>
0.15	–	–	1.35	900	< 1500	(3)	Hale Albite Rock

\* Frictional parameters:  $\mu$  = frictional coefficient,  $\tau_0$  = critical shear strength,  $\sigma_n$  = normal stress (eqn. 7);  $b$  = frictional coefficient,  $a$  = critical strength (eqn. 8).

\*\* Sources: (1) Byerlee (1978); (2) Stesky et al. (1974); (3) Shelton et al. (1981).

<sup>a</sup> Constructed from best-fit curves in fig. 11 of Stesky et al. (1974).

<sup>b</sup> As in (<sup>a</sup>), but based on few, scattered data points.

<sup>c</sup> Faults in vacuum-dried samples interpreted as shear cracks.

tion from the Byerlee (1978) coefficients occurs at higher pressures and temperatures for mafic crystalline rocks (e.g. Shimada et al., 1983). Stesky et al. (1974) attribute the temperature-dependent reduction in the frictional coefficients to conditions where the fracture strength exceeds the frictional strength and deformation is accompanied either by a change in fault configuration (i.e. broader fault zones) or by refaulting of the rock. Quite possibly, increased temperature dependence of  $\mu$  is related to the development of fault gouge or to the onset of crystal plasticity. Byerlee (1978, p. 625) states that his frictional coefficients (derived from a review of the literature) are valid for smooth sliding surfaces, initially interlocked surfaces or for geometrically irregular faults produced in initially intact rock. Time-, velocity- and displacement-dependent changes in  $\mu$  (e.g. Dietrich, 1978), the inter- and intragranular effects of water at crustal pressures and temperatures (Rutter and Mainprice, 1978; Shelton et al., 1981), and the influence of gouge along the fault surfaces (Shimamoto and Logan, 1981a, b) are all neglected. In addition, the role of subcritical crack-propagation (Atkinson, 1984) in promoting the localization of brittle failure is not considered. Despite these shortcomings, eqns. (7) and (8) and the Byerlee (1978) frictional coefficients are shown in the deformation regime maps to provide a good estimate of the range of pressures and temperatures over which frictional behavior predominates in the crust and uppermost mantle (Figs. 3–5 in the next section).

### 3. The nature of deformational topologies

#### 3.1. Pressure, pore pressure, temperature and grain-size effects

The  $\log \dot{\gamma}$ – $T$ – $P$  deformational coordinate system shown schematically in Fig. 2 is constructed from different  $\log \dot{\gamma}$ – $T$  and  $P$ – $T$  sections (e.g. Fig. 3). The  $\log \dot{\gamma}$ – $T$  diagrams (Figs. 3a and b) are valid for constant pressure, pore pressure and grainsize while the  $P$ – $T$  maps (Figs. 3c and d) hold for constant shear strain rate, pore pressure and grainsize. The diagrams are contoured for

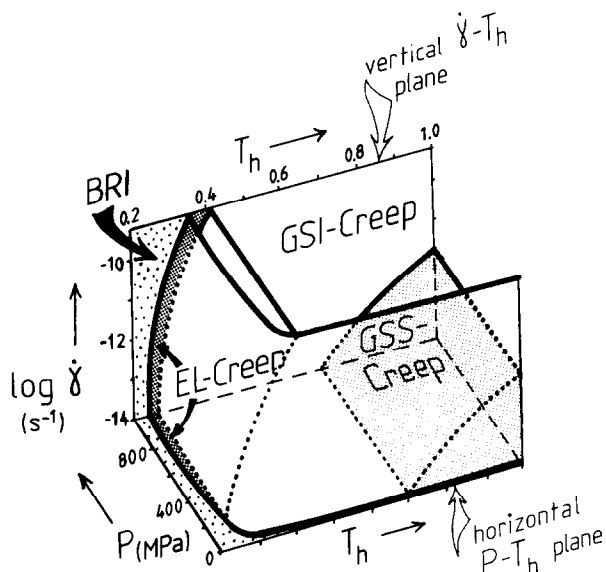


Fig. 2. Schematic  $\log$  shear strain rate ( $\dot{\gamma}$ )–homologous temperature ( $T_h$ )–pressure ( $P$ ) diagram showing the general position of mechanical equilibrium curves (thick solid lines) between brittle failure and frictional sliding (BRI, coarse stippling), exponential law creep (ELC, fine dark stippling), grainsize-insensitive power law creep (GSI, unstippled) and grainsize-sensitive power law creep (GSS, fine light stippling). The shape and relative position of the curves is based on Fig. 3 for hydrous dunite. The diagram is valid for constant grainsize and pore pressure.

differential shear stress and effective shear viscosity according to eqns. (A5)–(A8) in the Appendix.

Figures 2 and 3 indicate that the mechanical equilibrium curve separating brittle behavior from the viscous creep regimes is strongly dependent on strain rate and pressure. The temperature dependence of this regime boundary increases slightly with increasing strain rate (Figs. 3a and b) and increases considerably at low pressures ( $P < 100$ – $200$  MPa for  $\lambda = 0$ ; Figs. 3c and d). This increased pressure dependence at low pressures is probably more relevant to the deformational behavior of upper crustal lithologies, such as limestone and quartz-rich rocks, which have flow laws identical in form to, but with lower activation energies than, those used here for dunite. Changing the frictional constants from the values of Byerlee (1978) to the higher temperature and normal stress values of Stesky et al. (1974) results in only a marginal shift of the brittle–crystal-plastic equilibrium boundary to higher temperatures for a

given strain rate and pressure. The predicted 500–600°C temperatures at the brittle–crystal-plastic transition is in good agreement with the

estimated temperatures of this transition in naturally sheared olivine-rich mylonites, based on a correlation of syntectonic metamorphic mineral

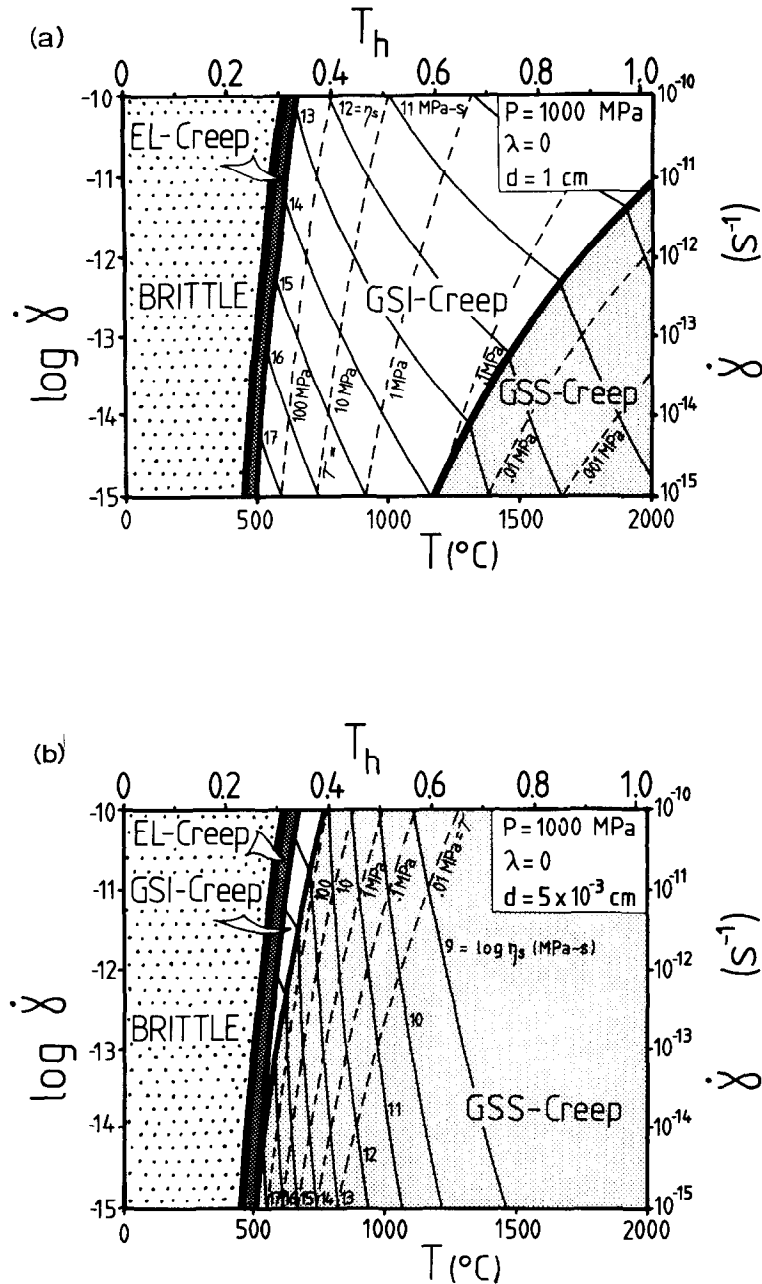
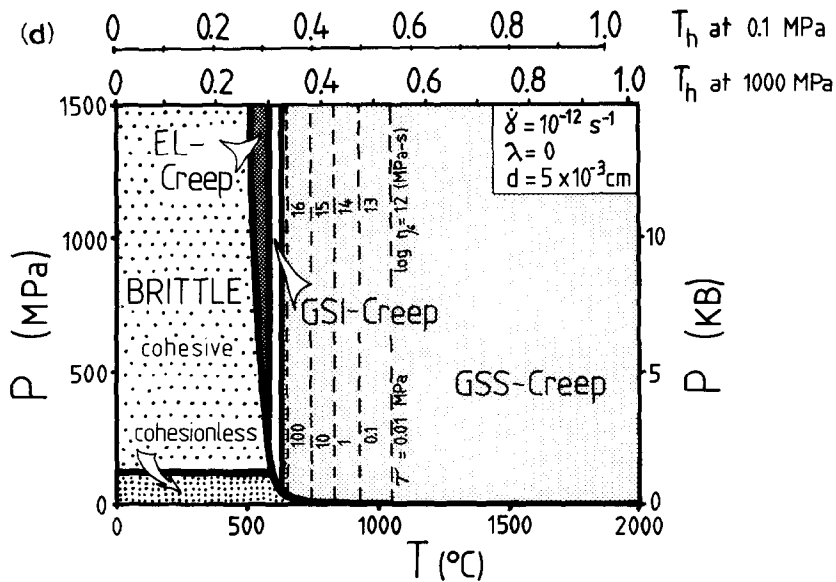
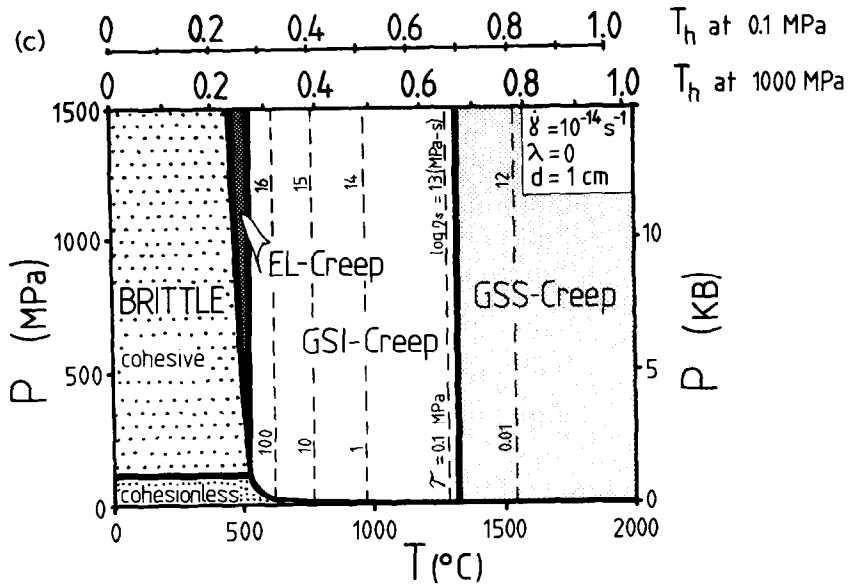


Fig. 3. Deformation regime maps for hydrous dunite. Log shear strain rate–temperature maps (a and b) and pressure–temperature maps (c and d) for zero pore pressure and two different grainsizes. Mechanical equilibrium fields are: brittle failure and frictional sliding (BRITTLE), exponential law creep (EL-Creep), grainsize insensitive power law creep (GSI-Creep). Contours in (a) and (b) are for shear stress (dashed lines) and effective shear viscosity (thin solid lines). Contours in (c) and (d) are for both shear stress and effective shear viscosity (eqns. A5–A8 in the Appendix). Homologous temperature,  $T_h$ , in (a) and (b) is corrected for pressure effects on the melting temperature (see Section 3.1). In (c) and (d),  $T_h$  is given for  $P = 0.1$  MPa (atmospheric pressure) and  $P = 1000$  MPa.



assemblages and microstructures (see Section 4.2).

Exponential law creep (ELC) occupies a relatively narrow domain in  $\log \dot{\gamma} - T - P$  space (Figs. 2 and 3), since it only describes the flow of rocks at the high differential stresses and low temperatures found near the transition from crystal-plastic to brittle deformation. Towards very low pressures typical of the upper crust, the exponential law creep-field pinches out and brittle behavior grades directly into the power law creep regimes (Figs. 3c and d). Interestingly, the boundary between ex-

ponential law creep and power law creep in Figs. 3a and 3b is almost parallel to the brittle-exponential law boundary curve. In fact, the curves diverge very slightly towards higher strain rates and smaller grain sizes (see Fig. 7 in the next section). The critical shear stress,  $\tau_c$ , at the transition from exponential law creep to power law creep in silicates is estimated at  $\tau_c \approx 10^{-2} G$  (where  $G$  is the temperature- and pressure-adjusted shear modulus) and shows only minor strain-rate dependence (Tsenn and Carter, 1987). Therefore, the  $\tau_c$

for olivine is ca. 800 MPa (Fig. 3;  $G$ -value of Kumazawa and Anderson, 1969). A higher estimate of  $\tau_c$  is obtained indirectly from eqn. (5) ( $\tau_c = \alpha = 1965$  MPa for hydrous Anita Bay dunite), but this value is less reliable due to the sparse high stress ( $> 500$  MPa) creep data for Anita Bay dunite, and to the implicit assumption in eqn. (5) that the activation energy of creep is equal in the low and high stress ranges (Tsen and Carter, 1987).

The steep slope of the curving shear stress- and viscosity-contours in Figs. 3a and b indicates that both the GSI and the GSS power law creep regimes are strongly temperature dependent. This dependence is greater at lower temperatures. Stated in other words, decreasing temperature at constant or near constant strain rate can lead to significant changes in the differential stress and viscosity. Such temperature-induced changes in flow stress during deformation are discussed in the next section in the context of strain localization.

Pressure effects on the power law creep regime are incorporated into the diagrams (Figs. 3, 4, 5 and 7) by relating the pressure sensitivity of creep to the pressure dependence of the melting (solidus) temperature (Weertman, 1970; Borch and Green, 1987):

$$\dot{\gamma} = \sqrt{3}^{n+1} A \exp\left(\frac{-gT_m}{T}\right) \tau^n \quad (10)$$

where  $T_m$  is the pressure dependent melting temperature (i.e. the slope of the solidus in the  $P$ - $T$  plane),  $1870^\circ\text{C}$  at  $P = 0.1$  MPa (Ashby and Ver-rall, 1978; Table 1);  $g$  is an experimentally determined constant.

This approach is more direct than the usual method of determining experimentally the activation volume that is appended to the apparent activation energy in eqns. (1), (2) and (5). \* The

experimentally determined slope of the solidus,  $dT_m/dP$ , for  $P$  up to 5000 MPa is  $0.07^\circ\text{C}/\text{MPa}$  (Nishikawa et al., 1970), so that increasing the pressure results in increased melting temperatures and, hence, in decreased homologous temperatures, decreased creep rates and increased viscosities for a given absolute temperature and applied stress in eqn. (10). Thus, at elevated pressures, there is a slight shift in the brittle-crystal-plastic equilibrium curve and the stress- and viscosity-contours to higher absolute temperatures and lower  $T_h$  (see  $T_h$  axes in Figs. 3c and d). Borch and Green (1987) point out that pressure probably also affects the other creep regimes in a similar way, since self-diffusivity is expected to show a pressure dependence which is analogous to that of creep and melting temperature. The physical basis for this relationship remains poorly understood pending further experimental verification.

Figures 3c and d indicate that pressure effects on GSI power law creep are minor for the effective pressure ranges considered in this paper ( $P_e \leq 1500$  MPa). Such effects are even less significant in crustal rocks such as quartzites and limestones since upper and intermediate crustal pressures are close, if not equal to, the confining pressures of the experiments. However, the activation volume and its pressure dependency become particularly important under lower mantle conditions where the pressures ( $> 10^5$  MPa) are of the same magnitude as the elastic moduli of the mantle minerals (see Poirier and Liebermann, 1984).

Grainsize-sensitive (GSS) creep is favored by small grainsizes, high temperatures and low strain rates and/or low stresses (compare Figs. 3a and c with Figs. 3b and d; see also Figs. 6 and 7 in the next section). Predictably, the boundary between GSI and GSS creep regimes is more temperature sensitive than either the brittle to crystal-plastic transition or the transition from GSI power law creep to exponential law creep. This reflects the combination of the relatively lower activation energy and lower stress-sensitivity of GSS creep. The GSI-GSS equilibrium boundary varies strongly with the assumed activation energy,  $Q$ , and grain-size exponent,  $m$  (Fig. 4). Figure 4 shows that an activation energy,  $Q_{\text{GSS}}$ , of  $0.67Q_{\text{GSI}}$  (297 kJ/mole) yields a more temperature-dependent equi-

\* The effective activation energy is defined as  $-(Q + \Delta PV^*)$ , where  $Q$  is the activation energy determined in the laboratory,  $V^*$  is the activation volume, and  $\Delta P$  is equal to  $P_L - P_c$ , the difference between the experimental confining pressure and the lithostatic pressure at a specified depth in the lithospheric section. Experimental values of  $V^*$  for olivine range from  $(1.1-4) \times 10^{-4}$  kJ/MPa-mole for confining pressures between 500 and 2700 MPa (Ross et al., 1979; Karato and Ogawa, 1982; Green and Hobbs, 1984).

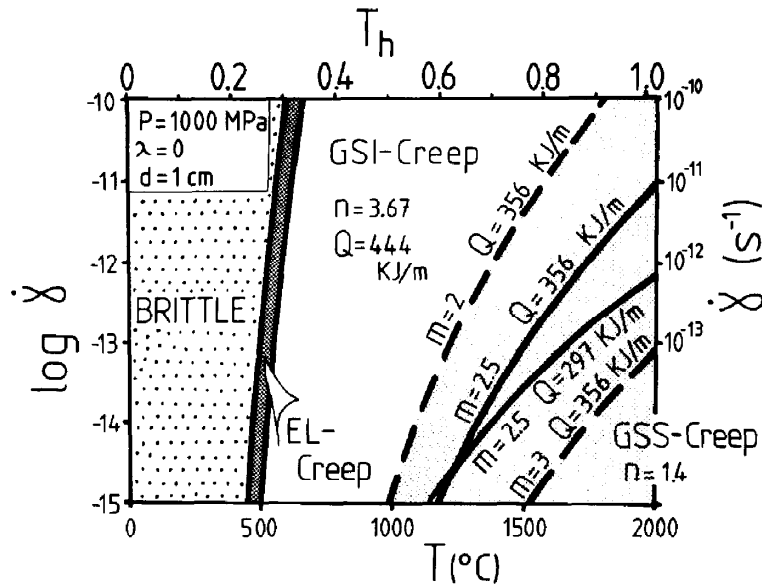


Fig. 4. Diagram for hydrous dunite at same conditions as in Fig. 3a, but showing the effects of varied activation energy of GSS creep,  $Q$ , and grainsize exponent,  $m$ , on the mechanical equilibrium curve between grainsize-insensitive (GSI) and grainsize-sensitive (GSS) power law creep.

librium curve than does the activation energy of 356 kJ/mole determined from hot-pressed olivine aggregates (Schwenn and Goetze, 1978). The same creep regime boundary is stable at much lower temperatures and strain rates for grain-boundary diffusion-accommodated grain-boundary sliding ( $m = 2$ ) than for volume diffusion-accommodated grain-boundary sliding ( $m = 3$ ; Fig. 4). Which accommodation mechanism predominates, depends primarily on the diffusivity and activation energy of diffusion of the rate-controlling species as well as on the width of the grain boundaries in the tectonites. Generally, for sufficiently low stresses and/or strain rates, very fine grains will favor grain-boundary diffusive processes over volume diffusion (see deformation mechanism maps for quartz in White, 1976). This is because effective grain boundary diffusivity is more grain-size dependent ( $\propto d^3$ ) than is effective volume diffusivity ( $\propto d^2$ ). The rheological implications of grainsize reduction and GSS-creep are examined more closely in Sections 4.2 and 4.3.

The brittle regime in Figs. 3c, d and 5 is subdivided into fields of cohesionless failure (at low pressures) and cohesive frictional sliding (at

higher pressures). The boundary between the two fields occurs at:

$$P = \frac{a_2}{(b_1 - b_2)(1 - \lambda)} \quad (11)$$

where  $b_1$  is the frictional coefficient at  $\sigma_n < 200$  MPa and  $a_2$  and  $b_2$  are the frictional constants at  $200 < \sigma_n < 1700$  MPa (eqn. 8 and the Byerlee frictional constants in Table 2). This depth and pressure-dependent subdivision reflects the general style and distribution of naturally occurring brittle tectonites: cohesionless fault gouges and breccias are generally found in shallow ( $< 2-4$  km) fault zones, while cohesive cataclasites are found in fault zones believed to have been active at depths between 4 and 10 km (Sibson, 1977). However, Donath et al. (1971) describe a more complicated transition from cohesionless to cohesive brittle behavior in experiments on limestone and marble at room temperature: with increasing pressure, extensional fracturing yields first to cohesionless brittle faulting, followed by localized cataclastic flow (their "ductile faulting"). At the highest pressures in their experiments (200 MPa), deformation involves uniform cataclastic flow on the scale of the laboratory specimens.

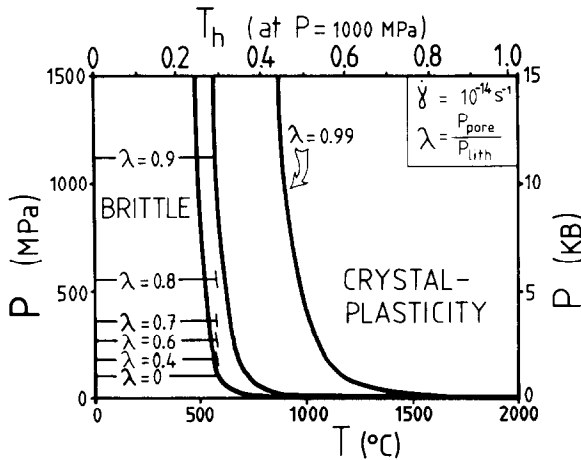


Fig. 5. Pressure ( $P$ )–temperature ( $T$ ) deformation-regime map for hydrous dunite at  $\dot{\gamma} = 10^{-14} \text{ s}^{-1}$  showing the effect of varied pore pressure ( $\lambda = P_{\text{pore}}/P$ ); see eqn. (9) in the text. The brittle field expands with increasing pore pressure (i.e. increased  $\lambda$ , or decreased effective pressure) at the expense of crystal plasticity.

Figure 5 demonstrates the influence of varied pore pressure,  $P_p$ , on the brittle–crystal-plastic transition. An increase in  $P_p$  (hence a decrease in effective pressure,  $P_e$ , according to eqn. 9) results in: (1) the displacement of the brittle–crystal-plastic equilibrium curve to higher pressures and temperatures for any given strain rate; (2) the movement of the cohesionless/cohesive frictional sliding boundary in the brittle regime to higher pressures (and hence to greater depths). The shift in the equilibrium temperature of the brittle–crystal-plastic boundary curve for dunite is  $\leq 100^\circ\text{C}$  for  $\lambda \leq 0.9$  (Fig. 5). Above this value, the brittle regime expands rapidly until at  $\lambda \geq 1.0$ , it covers the entire  $P$ – $T$  field. This implies that at  $P_p \geq P$ , deformation at all pressures and temperatures involves cohesionless brittle failure. Clearly, it is important when using such diagrams to specify the scale to which the deformation regime map applies. The highly nonlinear  $\lambda$ -dependency of the brittle–crystal-plastic equilibrium boundary in  $\log \dot{\gamma}$ – $T$ – $P$  space is due to the form of the equations (eqns. A1 and A2 in the Appendix) used to construct this curve. The maps suggest that rocks deforming in the field of crystal-plasticity can undergo sudden embrittlement if there are sufficiently large changes in the local pore pressure. If the rock is deforming just above the brittle to

crystal-plastic transition, even a modest fluctuation in  $\lambda$  (e.g. due to a syntectonic metamorphic reaction involving a volatile phase) can induce embrittlement. This may explain the localized occurrence of synmylonitic “crack-seal” veins in quartz-rich tectonites deformed under hydrous greenschist facies conditions (Handy, 1986; pl. 4.20).

### 3.2. Discrepancies between nature and experiments

Several points emerge when comparing the topologies of deformation regimes in  $\log \dot{\gamma}$ – $T$ – $P$  space with the conditions under which these deformation regimes are observed or inferred to operate in nature.

(1) Microstructural studies in naturally deformed rocks indicate that the boundary between deformation regimes is actually a transitional domain rather than an equilibrium curve on a deformation regime diagram. These domains are characterized by the overlapping effects of several mechanisms whose interaction determines the rheology of the rock. The transition from predominantly crystal-plastic to brittle behavior is inferred for most polymineralic rocks to involve concomitant crystal plasticity, reaction-enhanced granular flow, solution transport, and crack-seal dilation (e.g. Handy, 1986). The relative activity of these different mechanisms depends not only on the physical conditions of the deformation, but also on the strain-dependent changes in mineralogy, bulk chemistry and microstructure of the deforming rocks. The cyclical nature of these interactions inferred from microstructural and geochemical studies (e.g. White, 1977; Stel, 1986) suggests that mechanical behavior can be transient on the microscale, even though the bulk deformation remains in mechanical steady-state. A gradational domain separating brittle and crystal-plastic regimes is also broadly consistent with local yielding observed in high temperature frictional sliding experiments, a phenomenon which is attributed to incipient (transient?) plastic flow of asperities along the fracture surfaces (Mogi, 1974). This transition becomes broader at higher temperatures, above a certain pressure which is dependent on lithology (Stesky et al., 1974).

The interaction of mechanisms also occurs at the transition from GSI to GSS creep. Natural, nonuniform grainsize distributions can extend the effect of dislocation-creep well into the diffusion-creep field, and vice-versa, due to inhomogeneous stresses and/or strain rates on the granular scale (Freeman and Ferguson, 1986).

(2) Figure 5 shows how pore pressure promotes cohesionless brittle failure and expands the brittle field with respect to the viscous creep fields. Yet little is known in nature about its variation with depth. A simple approximation sometimes used is:

$$\lambda = \frac{P_{\text{pore}}}{P} = \frac{\rho_w g z}{\rho_r g z} \approx 0.4 \quad (12)$$

where  $\rho_r$  is the average density of the rock (2.8 g/cm<sup>3</sup>);  $\rho_w$  is the density of water (~1 g/cm<sup>3</sup>);  $g$  is the acceleration due to gravity (981 cm/s<sup>2</sup>);  $z$  is depth.

This equation assumes perfect interconnectivity of pore space and therefore is probably only valid for small strains, low strain rates and at depths above the onset of diagenesis (ca. 3 km). Below this level, the occurrence of metamorphic reactions and/or melting that involve a volatile phase can lead to local fluctuations in pore pressure. Also, dilatancy during cataclasis is associated with localized hardening and weakening as cracks are opened and sealed and pore pressure varies on the scale of the fault zone (e.g. Rutter, 1972). Generally, the law of effective stress (eqn. 9) only applies when the strain rate is sufficiently low in relation to the permeability of the deforming rock (Rutter, 1972). For these reasons, no crustal pore pressure gradient was assumed in the construction of the diagrams in Section 5.

#### 4. Strain localization and the rheological evolution of faults

##### 4.1. Temperature and grainsize effects

The localization of strain into fault zones results from the development of rheological instabilities that are broadly related to: (1) the inherited mineralogical and microstructural inhomogeneities of the rock; (2) the scale of these inhomogeneities with respect to the scale (magnitude) and

anisotropy of the stress field at the onset of deformation; and (3) the change in physical conditions during the deformation. While the deformation regime maps do not describe the initial boundary conditions of deformation [(1) and (2) above], they can be used to track the rheological feedback to the boundary conditions during strain localization. Temperature and grainsize are chosen as independent variables in the diagrams for this section because most mineral stabilities and creep processes are strongly temperature-dependent and grainsize is an important, measurable microstructural parameter. Although strain and time are not treated independently in the diagrams, both variables are implicit in the concept of a *rheological trajectory* during shearing (i.e. an evolution of mechanical conditions). They are considered again in the context of microstructural stability in Section 4.5.

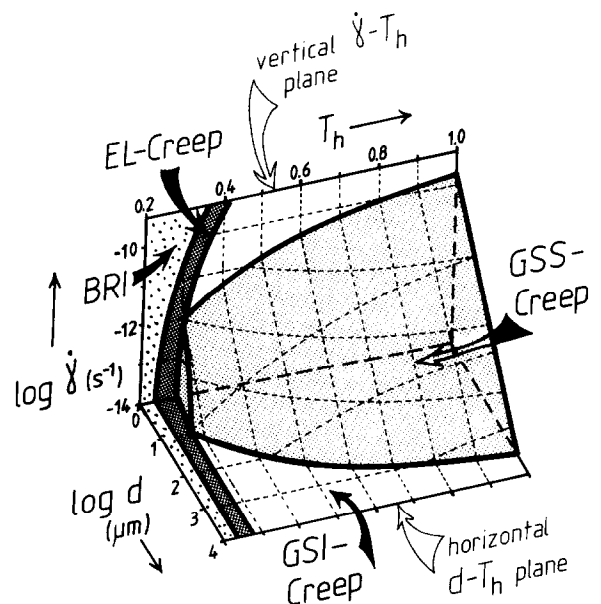


Fig. 6. Schematic log shear strain-rate ( $\dot{\gamma}$ )-homologous temperature ( $T_h$ )-log grainsize ( $d$ ) diagram showing the mechanical equilibrium curves (thick solid lines) between brittle failure and frictional sliding (BRI, coarse stipples), exponential law creep (ELC, fine dark stipples), grainsize-insensitive power law creep (GSI, unstippled) and grainsize-sensitive power law creep (GSS, fine light stipples). The surfaces of the diagram and the equilibrium plane separating GSI- and GSS-creep are contoured (dashed lines) for constant shear strain-rate, temperature, and grainsize. The shape and position of the equilibrium curves are based on Figs. 3a, b and 7 for hydrous dunite. The diagram is valid for constant lithostatic and pore pressure.

The strong grainsize and temperature dependencies of GSS creep referred to in the last section are seen more clearly in the schematic  $\log \dot{\gamma} - T - \log d$  diagram in Fig. 6 and the  $T - \log d$  deformation regime maps for wet dunite deforming at two different strain rates in Figs. 7a and b. The surfaces in Fig. 6 are contoured for strain rate, temper-

ature, and grainsize while the  $T - \log d$  maps in Fig. 7 are contoured for differential shear stress and effective shear viscosity. All three figures contain a grainsize-independent brittle field, valid (in Fig. 7) for a pressure of 1000 MPa at  $\lambda = 0$ . The figures show that, at a given strain rate, small grainsizes and high temperatures favor GSS creep.

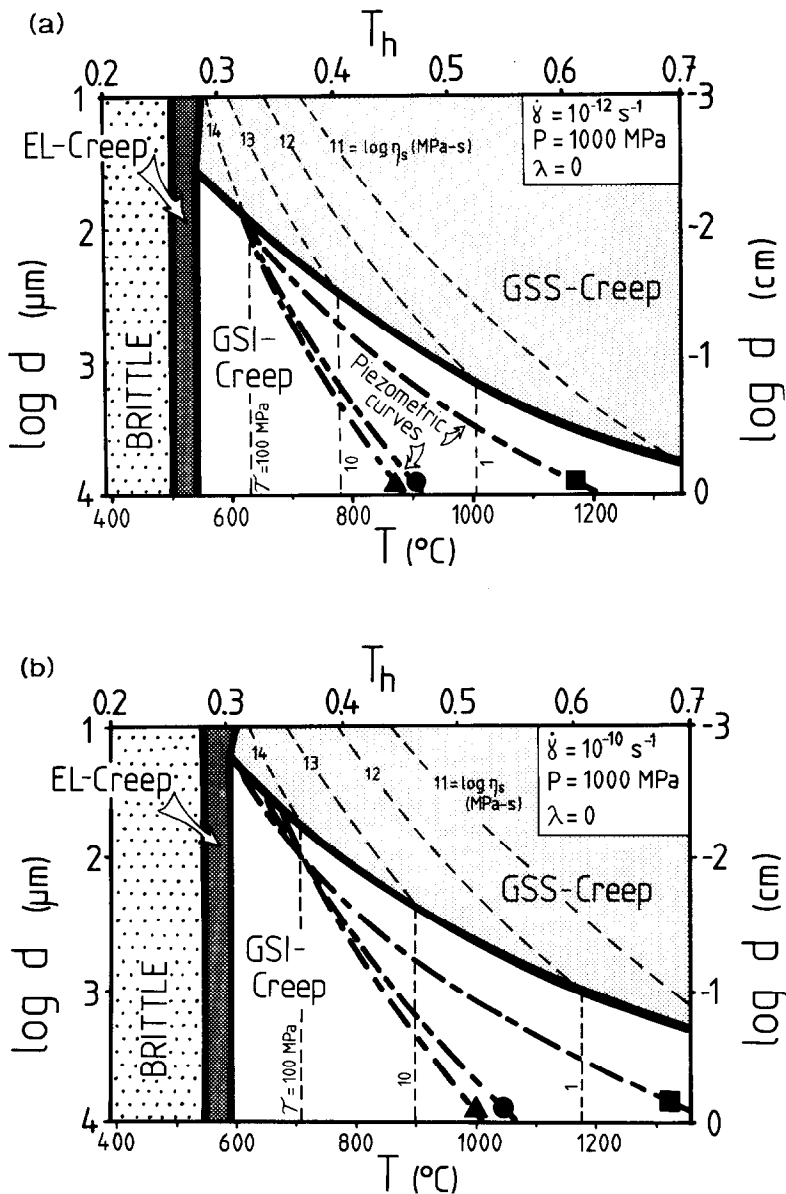


Fig. 7. Temperature ( $T$ )-log grainsize ( $d$ ) deformation-regime maps for hydrous dunite deforming at constant strain-rate, pressure and pore pressure. Mechanical stability fields are: brittle failure and frictional sliding (BRI), exponential law creep (ELC), grainsize-insensitive power law creep (GSI) and grainsize-sensitive power law creep (GSS). The contours of the creep fields are for shear stress and effective shear viscosity (eqns. A5–A8 in the Appendix). Piezometric curves are from: Post (1977; triangle); Mercier et al. (1977; circle) and Ross et al. (1980; square).

Similar conclusions are reached if the creep laws are depicted in stress–grainsize (Mohammed and Langdon, 1974) or stress–temperature coordinates (Stocker and Ashby, 1973) contoured for strain rate.

The relevance of GSS creep in tectonic processes is that enormous volumes of crust and mantle can be moved large distances along relatively narrow, high-strain shear zones far more efficiently than if GSI creep operates alone (e.g. Glarus overthrust; Schmid, 1975). This is because GSS creep at a constant or nearly constant strain rate involves flow at much lower stresses and viscosities than does GSI creep. However, most rocks have an initial grainsize which is too big for the diffusion-accommodation processes involved in GSS creep to compete effectively with dislocation-glide and -climb predominating in GSI creep. GSS creep in rocks therefore only occurs after an initial strain involving significant grainsize reduction.

Most natural tectonites deformed at homologous temperatures,  $T_h$  ( $= T/T_{\text{melting}}$ ), of greater than 0.2 display microstructural evidence of dynamic recovery and recrystallization: e.g. strong lattice preferred orientation (lpo), unstable sutured grain boundaries, dislocation substructures, and grainsizes larger than 10 to 20  $\mu\text{m}$ . To date, fabrics suggestive of predominant GSS creep in naturally deformed rocks (e.g. weak to nonexistent lpo, equant to subequant polygonal grains, grainsizes finer than 10  $\mu\text{m}$ ) have been identified in a limited number of rock types and tectonic environments: (1) polymineralic tectonites which have undergone syntectonic metamorphic reactions; (2) polymineralic tectonites deformed at moderate to high homologous temperatures and presumably low ambient stresses (SP-mylonites of Boullier and Gueguen, 1975); (3) monomineralic tectonites in low homologous temperature shear zones (e.g. anchizone marble mylonites; Schmid, 1975; Heitzmann, 1987; greenschist facies quartzite mylonites; Behrman, 1985). First, we shall consider the third type of occurrence since it pertains to the simplest case of a deforming rock whose rheology is governed by the flow of one relatively weak mineral. Cases (1) and (2) involving polymineralic tectonites are treated in Section 4.3.

#### 4.2. Strain localization in monomineralic tectonites

The restriction of GSS creep in monomineralic mylonites to low homologous temperatures and high stress conditions suggests that the lower temperatures and pressures typical of intermediate to upper crustal conditions favor grainsize sensitivity of creep. Yet the deformation regime maps in Fig. 7 indicate that GSS creep is enhanced at high temperatures due to the highly positive temperature-dependence of the diffusion-accommodation mechanism inferred for GSS creep. This apparent contradiction has been explained by the idea that significant grainsize reduction of a rock deforming in the GSI (dislocation creep) regime can induce a mechanism switch to GSS creep (Watterson, 1975; White, 1976), even at low temperatures.

Some end-member rheological trajectories in the GSI space leading to GSS creep are shown in Fig. 8. Experimentally calibrated, dynamically recrystallized grainsize piezometers for wet dunite are plotted in Figs. 7a and b and are depicted schematically as the curved plane labelled *P* in Figs. 8a and b. This piezometric surface follows the stress contours at different grainsizes according to the relationship (Twiss, 1977):

$$d = K\sqrt{3} \tau^{-p} \quad (13)$$

where  $d$  is the dynamically recrystallized grain-size,  $\tau$  is the differential shear stress,  $K$  and  $p$  are material constants with only a small, if at all existent, temperature dependence; and  $\sqrt{3}$  was defined in eqn. (3).

In the GSI space of Fig. 8, the stress- and viscosity-contours run parallel to the temperature contours on all surfaces except the  $\log \dot{\gamma} - T_h$  plane (see Figs. 3 and 7). Stress increases towards lower  $T_h$ . The rheological trajectories all begin with a volume of deforming rock at an initial hypothetical grainsize of  $10^4 \mu\text{m}$  (1 cm).

Twiss (1976) and Etheridge and Wilkie (1979) have argued that grainsize reduction in the GSI-field tracks with according to eqn. (13). A constant strain rate variant of this trajectory is shown as path  $A_0-A_1$  in Fig. 8a. An interesting consequence of this model trajectory is that steady-state, stress-dependent grainsize reduction in the GSI

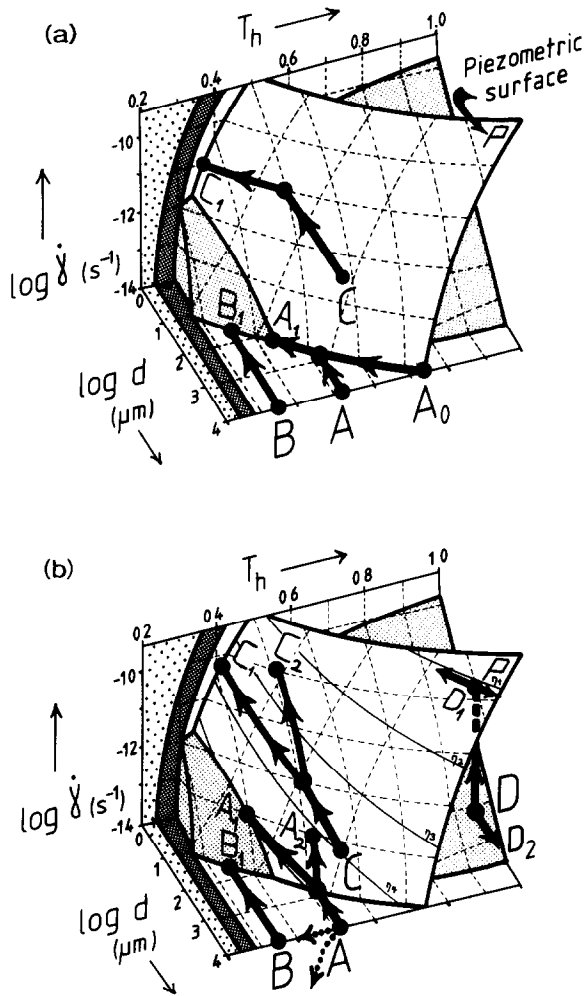


Fig. 8. End-member rheological evolution paths for deforming rocks whose rheology is governed by the flow of one weak mineral. Schematic log shear strain-rate ( $\dot{\gamma}$ )-homologous temperature ( $T_h$ )-log grain size ( $d$ ) diagrams are valid for constant lithostatic pressure and pore pressure. The mechanical stability fields are signified as in Fig. 6. Plane  $P$  represents the equilibrium piezometric relationship between flow stress and dynamically recrystallized grain size in the GSI field (eqn. 13). All surfaces in the GSI and GSS creep fields are contoured for constant shear strain-rate, temperature and grain size. The piezometric surface in (b) is also contoured for constant effective shear viscosity (thin solid lines).

a. Grainsize-reduction paths at constant shear strain-rate (see Section 4.2 for explanation). Note that grainsize reduction in the GSI creep field involves dynamic recrystallization. The GSS creep field is only "seen" by a deforming rock at low temperatures and small grain sizes.

b. Grainsize-reduction paths at constant or decreasing shear viscosity. Dashed line is that part of the rheological path occurring behind the piezometric plane. Dotted lines at  $A$  are possible rheological trajectories of rocks outside of the fault zones (see Section 4.5).

regime which leads to GSS creep can only occur under retrograde conditions (Fig. 8a). This is plausible in light of the field observations cited above, but it seems geologically more realistic to postulate a rheological path with an initial grain-size above the stress-dependent, dynamically recrystallized grain size ( $A-A_1$  in Figs. 8a and b). Dynamic recrystallization leads to a drastic grain-size-reduction after only small amounts of strain (see discussion in 4.5 below) until the trajectory intersects the piezometric plane and equilibrates with the flow stress. GSS creep initiates at a strain rate, stress, temperature and grain size where the piezometric surface in Figs. 8a and b intersects the equilibrium boundary between GSI and GSS creep. Within the GSS space, dynamically recrystallized grain size no longer tracks with stress and eqn. 13 is not valid. Rheological trajectories in the GSS regime are considered in Section 4.4 (Figs. 13a and b). Path  $C-C_1$  in Figs. 8a and b shows that for a sufficiently high strain rate, no transition to GSS creep need occur. The deformation remains entirely within the field of GSI creep until it intersects the crystal-plastic-brittle transition at some small grain size and low homologous temperature (behind the  $\log \dot{\gamma} - T$  plane in Fig. 8).

These constant strain rate and constant viscosity paths along the piezometric surface in Figs. 8a and b only represent end-member rheological paths for shear zones which are active over lengths of time comparable to changes in the ambient temperature. Many shear zones probably develop at isothermal or near isothermal conditions. Schmid (1982) proposes that mylonitization at sufficiently low ambient temperatures can result in a mechanism switch to GSS creep without the microstructure ever equilibrating with the flow stress (path  $B-B_1$  in Figs. 8a and b). This rheological path is probably more common in intermediate to shallow lithospheric levels (Section 5.1). More generally, strain localization in the GSI regime involves a decrease in viscosity and hence, leads to a rapid increase in strain rate with increasing stress (paths  $A-A_2$  and  $C-C_2$ ). Under such conditions, a transition to GSS creep is not possible according to the configuration of mechanical equilibrium curves in Fig. 8b.

In some tectonites, the grain size may be below



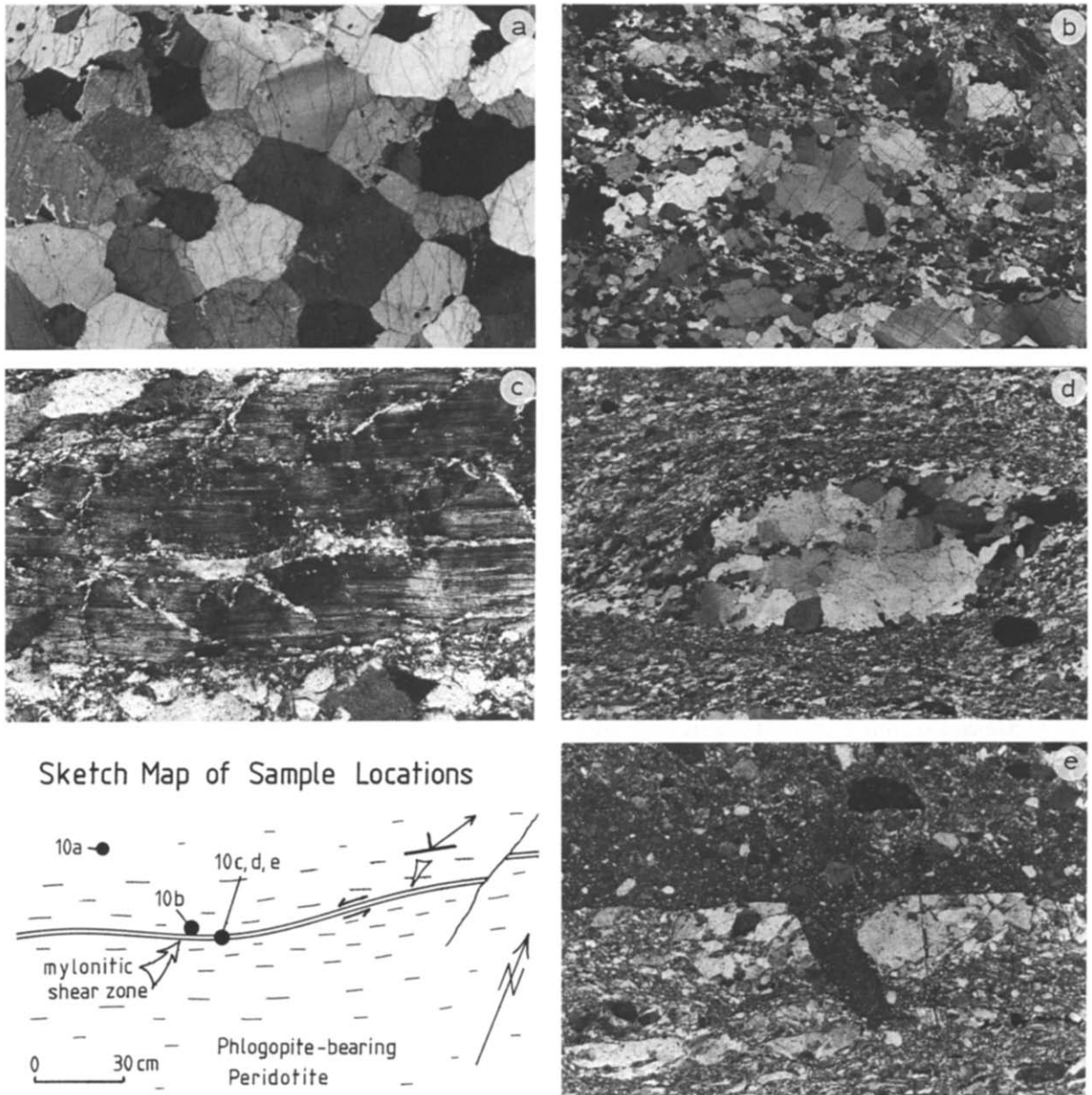


Fig. 10. Microstructural evolution within a sheared phlogopite-bearing peridotite from the Finero Complex in the Ivrea Zone of northwestern Italy.

- a. Microstructure within a weakly foliated peridotite outside of the shear zones. Note the large olivine grainsize (ave. 1–2 cm) and equilibrated grain boundaries. Undulose extinction is probably related to shearing in (b)–(d) below. Narrow transgranular cracks are associated with late brittle deformation (see e). Frame dimensions: 11.5 × 7.7 mm.
- b. Mylonitic microstructure within the shear zones: matrix of dynamically recrystallized olivine (ave. grainsize ca. 50–100 μm) surrounds clasts of un- or less-recrystallized olivine, orthopyroxene, amphibole, and phlogopite (11.5 × 7.7 mm).
- c. Incipient syntectonic alteration of an orthopyroxene clast to phlogopite is concentrated along intragranular cracks (0.7 × 0.5 mm).
- d. Ultramylonitic microstructure at the center of the shear zones; ultramylonitic matrix is comprised of fine-grained (~10 μm) syntectonic phlogopite and olivine and contains a boudinaged clast of dynamically recrystallized olivine (5.6 × 3.8 mm).
- e. Ultramylonitic foliation (bottom) is locally overprinted by cataclasites and ultracataclasites (top). Note the “intrusion” of ultracataclastic material into the surrounding ultramylonite (1.4 × 1.0 mm).

the geothermometer and the measuring technique (Brodie, 1980; Zingg, 1983).

In the sample located just adjacent to the shear zone (i.e. 3 cm from the center of the shear zone), olivine has undergone extensive dynamic recrystallization and forms a matrix of fine grains (3–75  $\mu\text{m}$ , Kruhl and Voll, 1978–1979, p. 106) which surround unrecrystallized olivine and orthopyroxene clasts (Fig. 10b). The development of a strong lattice preferred orientation in dynamically recrystallized olivine grains such as these (e.g. 001-axes parallel to the mylonitic stretching lineation, see type-IV patterns on p. 96 of Kruhl and Voll, 1978–1979), indicates that GSI power law creep of the olivine aggregates controlled the rheology of the rock at this stage. Incipient reaction of the hornblende and orthopyroxene (opx) to fine-grained phlogopite is apparent along the fractures in the clasts (Fig. 10c) and implies the infiltration of a hydrous fluid phase during shearing (Brodie, 1980).

The tectonite taken from the center of the shear zone (Fig. 10d) contains an ultrafine-grained (5–10  $\mu\text{m}$ ) matrix of syntectonically recrystallized phlogopite and olivine  $\pm$  opx. The boudinage and elongation of dynamically recrystallized olivine aggregates (Fig. 10d) indicates that a strength inversion has occurred between the dynamically recrystallized olivine grains and the micaceous reaction products. This is due to the fine grain size of the syntectonic phlogopite and to the suppression of equilibrium grain growth of olivine in the matrix. It is the fine-grained phlogopite-rich matrix which now controls the rheology of the deforming rock. While the microstructural evolution shown in Fig. 10 occurred in a peridotite, similar trends are observed in ortho- and paragneisses deformed under eclogite facies conditions (Rubie, 1983) and amphibolite to greenschist facies conditions (Handy, 1986). Cataclasites and ultracataclasites within the ultramylonites (Fig. 10e) mark late brittle movements. In this case, it is not possible to ascertain whether embrittlement was continuous with the final stages of retrograde crystal-plastic deformation, or if it represents the reactivation of the shear zone under anchizone conditions or lower.

The  $\log \dot{\gamma} - T - \log d$  diagram in Fig. 11 depicts the possible rheological evolution of a deforming rock which has undergone a syntectonic reaction such as that outlined above for the sheared peridotites in the Ivrea Zone. The diagram is like that in Fig. 8, but includes an isothermal plane,  $R_x$ , representing a syntectonic reaction at temperature  $T_h = 0.5$ , and pressure  $P$ . End-member rheological paths for constant strain rate (path  $ABCD$ ) and constant viscosity (path  $ABEF$ ) are shown, but only the latter is described here. Initial dynamic recrystallization of olivine along  $A-B$  is followed by a continuous stress-dependent grainsize reduction of olivine under retrograde conditions of increasing stress and strain rate along  $B-E$ . This corresponds roughly with the mechanical and thermal conditions inferred from the microstructures in Fig. 10b. At point  $E$  in Fig. 11, syntectonic reaction causes drastic grainsize reduction towards point  $F$ . This can lead to GSS creep if the syntectonic grainsize is sufficiently small and the

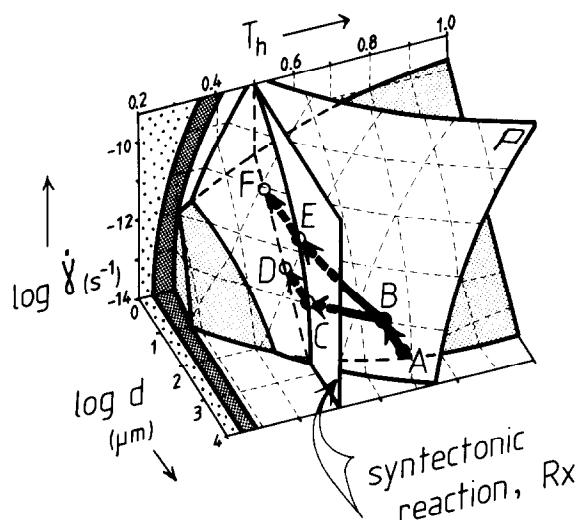


Fig. 11. End-member retrograde rheological evolution paths for polyminerale tectonites involving a syntectonic metamorphic reaction,  $R_x$ . Mechanical stability fields, equilibrium boundary surfaces and contours are the same as in Figs. 6 and 8. The location of the reaction plane,  $R_x$ , at a homologous temperature of 0.5 corresponds approximately with the conditions of syntectonic reaction in Figs. 10c and d (see text). Dashed lines and open circles represent points hidden from direct view. Paths  $ABCD$  and  $ABEF$  are, respectively, constant strain rate and constant viscosity paths (explanation in Section 4.3).

volume proportion of this fine-grained material is large enough. Such conditions may apply to the ultramylonites in Fig. 10d. Just how small the grainsize and how large the volume proportion of fine grains must be in order for GSS creep to predominate will depend on the effective diffusivity of the rate-controlling species in the mylonitic matrix relative to the dislocation mobility in, or brittle strength of, the less-deformed clasts.

Reaction-induced or -enhanced softening can occur under either retrograde or prograde metamorphic conditions. However, this process is seen as the most effective, and probably also the predominant mode of concentrating strain in polymineralic rocks in a prograde tectonic environ-

ment. In the absence of such prograde reactions, rates of dislocation climb and grain growth increase with temperature and work against the localization of strain (i.e. shear zones will broaden and deformation will become more diffuse). Enhanced dislocation mobility hinders the reduction of grainsize to the levels required for GSS creep. Together with grain growth and microstructural equilibration during post-tectonic anneal, this is probably why prograde shear zones are so rarely recognized in nature.

A simple example of a constant strain-rate prograde rheological trajectory is shown in the diagrams in Fig. 12. Initial grainsize-reduction in the weakest mineral of the tectonite proceeds from *A* as far as the equilibrium grainsize *B*. Thereafter, grainsize increases along the piezometric curve until temperatures are attained that correspond to the discontinuous reaction at point *C* on the plane *R<sub>x</sub>*. Two end-member paths leading to GSS creep, *C-D* and *C-E*, are possible: path *C-D* involves a grainsize decrease during reaction which is sufficiently great to induce GSS creep at the *P-T* conditions of the reaction. For the alternative path, *C-E*, the growth of the new syntectonic reaction product(s) suppresses equilibrium grain growth of the initially weak mineral. Continued deformation with increasing temperature occurs at constant grainsize until the rock intersects the GSI-GSS regime boundary and begins to deform by GSS creep.

#### 4.4. Rheological trajectories in the grainsize-sensitive creep field

A change from GSI (dislocation) creep to diffusion-accommodated GSS creep will occur if three fundamental conditions are fulfilled: (1) the grainsizes within the GSI-creep field are sufficiently small; (2) temperatures are low enough to retard significant grain growth, but remain high enough to allow grain-boundary diffusion; (3) the fine grains comprise a significantly high proportion of the rock (> 30 vol.%; Jordan, 1987) to govern its rheology. Once these conditions are met, drastic softening will occur due to the lower stress sensitivities and activation energies of GSS creep.

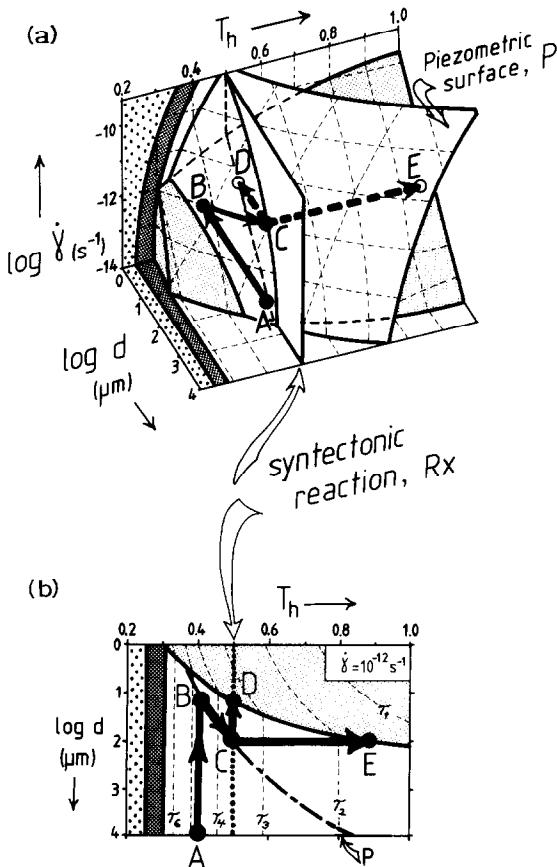


Fig. 12. Prograde, constant strain rate rheological evolution path for polymineralic tectonites involving a syntectonic reaction, *R<sub>x</sub>*. The mechanical stability fields, equilibrium boundary surfaces, and contours in (a) and (b) are identical to those in Figs. 11 and 9, respectively. See end of Section 4.3 for explanation.

Within the field of GSS creep, there are several end-member rheological paths that result in changes in flow stress and/or strain rate. These are illustrated in Fig. 13, in which the GSS-creep field has been exposed to reveal the curved planes of constant flow stress: (1) If mechanical and

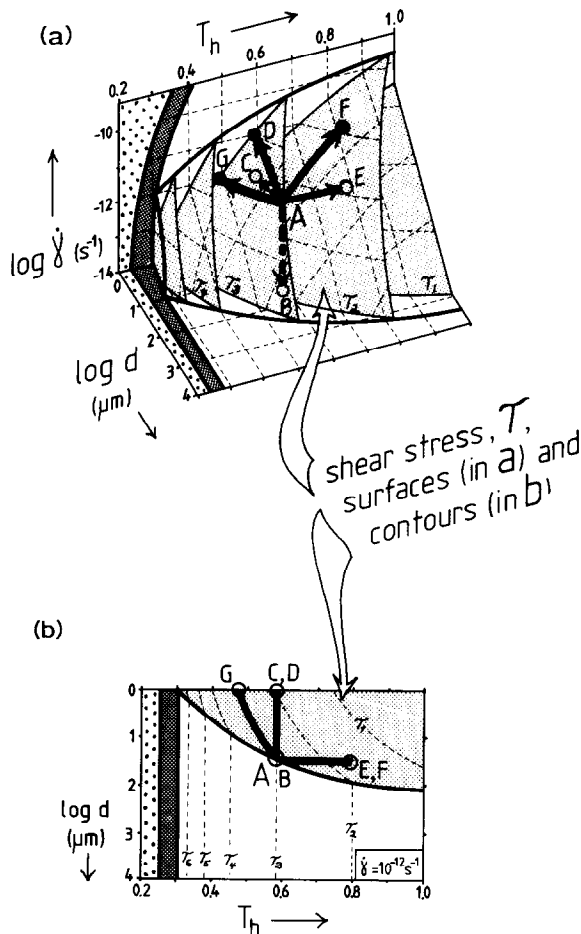


Fig. 13. End-member rheological paths within the field of grainsize-sensitive (GSS) power law creep. All rheological paths start from point A on the mechanical equilibrium boundary between the GSI- and GSS-creep regimes (see Section 4.4 for explanation).

a. Schematic log shear strain rate ( $\dot{\gamma}$ )–homologous temperature ( $T_h$ )–log grainsize ( $d$ ) diagram as in Fig. 6, but containing curved planes of constant shear stress (fine light stipples) within the GSS-creep field. Shear stress increases from  $\tau_1$  to  $\tau_5$ . All surfaces are contoured for constant strain rate, temperature, and grainsize.

b. Temperature ( $T$ )–log grainsize ( $d$ ) diagram at  $\dot{\gamma} = 10^{-12} \text{ s}^{-1}$  is derived from Fig. 12a. Mechanical stability fields and contours are identical to those in Fig. 13b and are based semiquantitatively on Fig. 7a.

microstructural equilibria are achieved (e.g. following path  $A-A_1$  in the GSI-creep field of Fig. 8), then GSS creep may involve a stress and strain-rate drop at constant grainsize (path  $A-B$  in Fig. 13). This trajectory is based on the experiments of White et al. (1985) on polycrystalline magnesium in which a stress drop occurs at a dynamically recrystallized grainsize that remains in equilibrium with the peak stress. (2) Decreasing grainsize at constant temperature and strain rate leads to a stress decrease along path  $A-C$ . (3) Decreasing grainsize at constant temperature and stress requires an increase in strain rate along path  $A-D$ . (4) Under syntectonic prograde conditions in the GSS-creep regime, deformation at constant grainsize can progress along path  $A-E$  at constant strain rate and decreasing stress or along path  $A-F$  at constant stress and increasing strain rate. (5) Deformation in the GSS regime which involves decreasing grainsize at constant stress and strain-rate (i.e. constant viscosity) can only occur under syntectonic retrograde conditions (path  $A-G$ ).

Note that paths  $A-C$ ,  $A-D$ ,  $A-E$  and  $A-F$  in Fig. 13 all result in a decrease in viscosity. Path  $A-B$  involves a viscosity increase, since the strain rate decreases more rapidly than does stress at constant temperature and grainsize (see eqn. 1 and contours in Fig. 3). This rheological trajectory probably pertains to ductile shear zones at or near the end of their movement history.

#### 4.5. The effects of time and strain on fault zone rheology

When considering the model rheological trajectories above, it is helpful to recall the time and size scales of the dynamic processes involved in ductile faulting. The straight, essentially isothermal grainsize-reduction paths in the GSI-creep regime in Fig. 8 represent changes in the microstructure that occur after very small strains and short times. In high-temperature creep experiments, mechanical and microstructural steady-state are achieved following critical shortening strains of as little as 5 to 10% (A. Ord, written commun., 1985). If homogeneous shear is assumed on the scale of the shear zone, a pure shear strain

of 0.100 corresponds to an octahedral simple shear strain,  $\gamma$ , of only 0.173 (eqn. 4). For average shear strain rates of  $10^{-12}$  to  $10^{-13}$  s $^{-1}$ , this critical shear strain is attained after only:

$$t_{\text{years}} = \frac{\gamma}{\dot{\gamma}}$$

$$= \left[ \frac{0.173}{(10^{-12} - 10^{-13} \text{ s}^{-1})(3.15 \times 10^7 \text{ s/yr})} \right]$$

$$= 5.5 \times 10^3 \text{ to } 5.5 \times 10^4 \text{ years} \quad (14)$$

This is a maximum estimate, since faster strain rates and critical strains of <10% are possible. Similarly, the isothermal syntectonic reaction-induced grainsize-reduction paths (*C-D*) in Figs. 11 and 12 imply that the reaction rate must be fast compared to the strain rate. In contrast, those parts of retrograde rheological trajectories in which grainsize tracks with stress (e.g. paths *A-A*<sub>1</sub> and *C-C*<sub>1</sub> in Figs. 8a and b) require much longer times and involve temperature changes that are presumed to occur over periods comparable to the duration of deformation. For example, a ductile shear zone with a finite simple shear strain,  $\gamma$ , of 100 to 1000 deforming at an average shear strain rate of  $10^{-12}$  s $^{-1}$  is active for ca. 3.2 to 32 m.y., using eqn. (14) above. Shear strains of 100 to 1000 correspond to displacements of between 8.9 and 89 m for a meter-wide shear zone. These values limit the shear strain in many large fault zones. Uplift rates in orogenic terrains can occur over similar time spans. Indeed, the activity of large shear zones is closely related to, if not directly responsible for, the late cooling history of some metamorphic terrains (e.g., the Insubric Line; Hurford, 1986; Schmid et al., 1987).

The rheological paths in the deformation regime diagrams are valid only for the scale of the ductile shear zones. As the shear zones nucleate and evolve, the volume of rock outside of the shear zones undergoes a much different rheological history. This is shown with the dotted lines in Fig. 8b for the rheological trajectories beginning at point *A*. The dotted lines indicate that strain rate in the large, less deformed volume of rock outside of the shear zone decreases or remains constant as the strain is localized into ductile shear zones. Constant or decreasing strain rate

under isothermal or retrograde conditions results in a viscosity increase (see contours in Fig. 3a). In comparison, the rheological evolution of shear zones involves a lower rate of viscosity increase or even conditions of constant or decreasing viscosity (paths *A-A*<sub>1</sub> and *A-A*<sub>2</sub> in Fig. 8b) with concomitant relative increases in stress and strain rate. So the localization of strain under either isothermal or retrograde conditions is associated with a strain- and/or temperature-dependent increase in the viscosity contrast between the shear zone and the surrounding, less deformed rock. Based on the configuration of the viscosity contours in Figs. 3 and 7, it is evident that this viscosity contrast becomes more pronounced at lower temperatures. This explains why, for a given rock type, low-temperature shear zones are narrower and have higher strain gradients towards the adjacent rock than higher-temperature shear zones (e.g. observations in Ramsay, 1980).

## 5. Detachment and shear in the lithosphere: an evolutionary rheological model

### 5.1. The boundary conditions

The effects of changing pressure, temperature and grainsize on the rheological history of fault rocks bear important implications for the structure and rheology of the Earth's lithosphere. The tectonic model presented in this section is intended to demonstrate the potential effects of interactive microstructural and metamorphic processes in the evolution of a simple lithospheric section. While this model pertains to an extensional tectonic setting, the general principles are also valid for a compressional tectonic environment.

Consider a hypothetical lithospheric section comprised of three lithological domains whose rheology is governed, respectively, by wet quartzite (granitic upper crust, UC), dry quartzite (granodioritic lower crust, LC) and wet olivine (olivine-rich uppermost mantle, UM). For the sake of simplicity, the lithological domains are assumed to be compositionally homogeneous on the scale of the section. The depth to the Moho prior to lithospheric stretching is set arbitrarily at 47 km.

Figure 14 superposes geothermal, petrological and rheological information for this model section. It contains a static, steady-state rift geotherm,  $Gr_{ss}$ , of Chapman (1986), two retrograde pressure–temperature–time ( $P$ – $T$ – $t$ ) paths, and two discontinuous reaction curves. Also included are deformation regime boundaries separating brittle behavior from GSI power law creep as well as shear stress and effective shear viscosity contours in the creep fields of the three lithological domains referred to above.

The retrograde  $P$ – $T$ – $t$  paths in Fig. 14 describe the thermobarometric history of crustal scale horizontal to subhorizontal fault zones at the interface between upper crust–lower crust (UC–LC, curve  $X_0$ – $X_4$ ) and lower crust–upper mantle (LC–UM, curve  $Y_0$ – $Y_4$ ). Each point along the

$P$ – $T$ – $t$  paths also represents a point along a unique transient geotherm, that is greater than the initial steady-state geotherm,  $Gr_{ss}$ . In the absence of complete  $P$ – $T$ – $t$  paths from natural shear zones in exhumed extensional terrains, the paths in Fig. 14 are constructed conceptually for an extending lithosphere in which the overall rate of heat loss due to conduction and advection is greater than the rate of heat increase resulting from the juxtaposition of hot, uplifted, and/or intruded material against cooler crustal rocks. In other words, the rate of thermal equilibration is relatively fast compared to the rate of extensional shearing, so cooling occurs throughout the time frame considered. This is reflected in the concave shape of the  $P$ – $T$ – $t$  curve, with a positive slope in the  $P$ – $T$  plane. Although the model is qualitative,

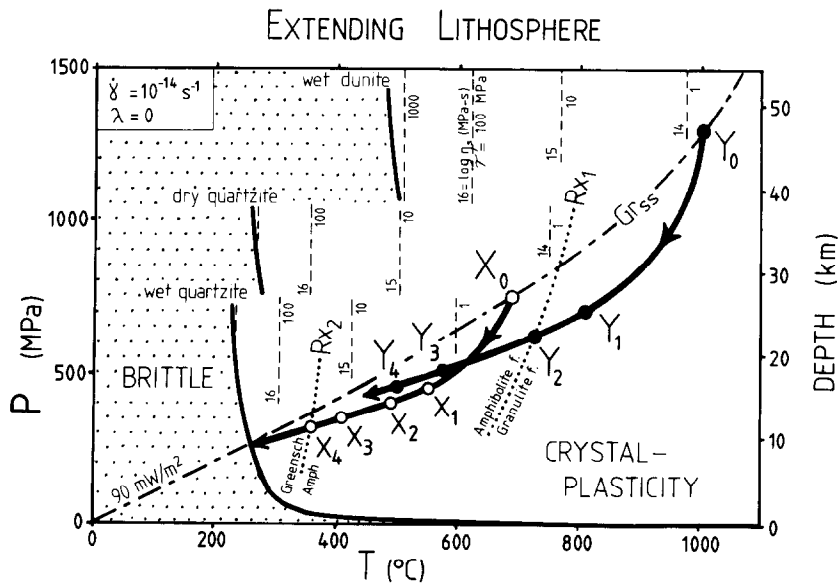


Fig. 14. Combined pressure–temperature deformation regime map and petrogenetic grid showing a model pressure–temperature–time rheological evolution during rifting of the upper continental lithosphere. Points  $X$  and  $Y$  coincide with large fault zones at lithological/mineralogical boundaries between upper crust, lower crust, and upper mantle. The rheological evolution of these fault zones is tracked through time,  $t_0$ – $t_4$ , in Fig. 15 (see text). Sources: Steady-state rift geotherm is modelled for a surface heat flow of 90  $\text{mW}/\text{m}^2$  (Chapman, 1986). Construction of model pressure–temperature–time trajectories is described in Section 5.1. Two generic syntectonic metamorphic reactions for aluminosilicate rocks of the continental crust:  $Rx_1$  is the reaction muscovite + quartz  $\rightleftharpoons$  Kfeldspar + Al-silicate +  $\text{H}_2\text{O}$  (prograde formulation; Turner, 1981), taken to separate the amphibolite facies from the granulite facies.  $Rx_2$  represents a hypothetical hydration reaction at the transition between greenschist facies and amphibolite facies. Mechanical equilibrium curves for the transition from brittle to grainsize-insensitive (GSI) power law creep and for contours of effective shear viscosity are valid for a regional shear strain rate of  $10^{-14} \text{ s}^{-1}$ . Frictional constants for the brittle regime are from Byerlee (1978; Table 2 this paper). Creep data: (1) wet Anita Bay dunite based on a reanalysis of steady-state creep data of Chopra and Paterson (1981; Table 1 this paper); (2) vacuum-dried Heavitree quartzite from Jaoul et al. (1984):  $A = 3.44 \times 10^{-6} \text{ MPa}^{-n} \text{ s}^{-1}$ ,  $n = 2.8$ ,  $Q = 184 \text{ kJ}/\text{mole}$ ; (3) hydrous “as is” Heavitree quartzite from Jaoul et al. (1984):  $A = 9.98 \times 10^{-6} \text{ MPa}^{-n} \text{ s}^{-1}$ ,  $n = 2.4$ ,  $Q = 163 \text{ kJ}/\text{mole}$ .

it produces a thermal history that approximates the geologically realistic concept of gradual, isostatically balanced lithospheric stretching (Lachenbruch et al., 1985).

The reaction curve,  $R_{x_1}$ , is the muscovite-breakdown hydration reaction in granitic and pelitic rocks and is taken to approximate the transition from the amphibolite to the granulite facies. Similarly, the hypothetical hydration reaction,  $R_{x_2}$ , separates greenschist from amphibolite facies conditions (Fig. 14).

Figure 15 shows the shear strength- and viscosity versus depth profiles corresponding to five points in time,  $t_0$  to  $t_4$ , along the  $P$ - $T$ - $t$  paths in Fig. 14. The shear zones (striped regions in Fig. 15) are assumed to maintain constant viscosity throughout their history. The consequences of this assumption are addressed in Section 5.6.

5.2. Initial strain localization at time  $t_0$

Strain localization in this very simple lithospheric column may occur at different times and depths and involve several of the rheological trajectories outlined in the last section. With the onset of deformation at time  $t_0$ , there are at least three type-localities of potential rheological instability (numbered in Fig. 15a): (1) at major lithological boundaries (e.g. boundaries between UC and LC at point  $X_0$  and between LC and UM at point  $Y_0$  in Fig. 15a); (2) at the high stress “beak” marking the transition from brittle behavior to viscous creep; (3) at depths corresponding to the intersection of the ambient steady state geotherm with the reaction curves. These rheologically unstable zones are considered in order below.

After only small amounts of strain and time (Section 4.5), dynamic recrystallization at the type (1) locations ( $X_0$  and  $Y_0$  in Fig. 15a) can lead to the development of ductile fault zones in the weakest parts, i.e. the base, of the less competent lithological units (UC and LC), but possibly also affecting the adjacent tops of the relatively competent units (LC and UM) at such lithological boundaries. Shear zones develop at these localities due to the differing activation energies and stress

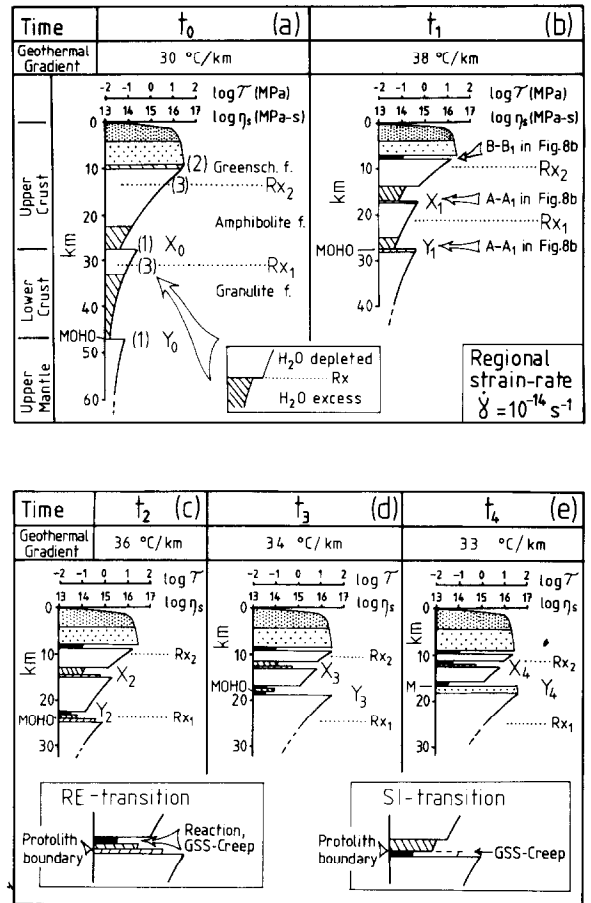


Fig. 15. Log shear strength and log effective shear viscosity versus depth profiles through a simple compositionally heterogeneous model of the continental lithosphere for various times ( $t_0$ - $t_4$ ) during rifting at a constant regional strain rate of  $\dot{\gamma} = 10^{-14} \text{ s}^{-1}$ . Profiles are constructed graphically from the rheological and model petrological information in Fig. 14. Numbers 1, 2 and 3 in Fig. 15a are zones of potential rheological instability described in the text (Section 5.2). Major fault zones (hatched regions) nucleate in parts of the crust with a shear strength of 1 MPa or less (points  $X$  and  $Y$ ) and are assumed to remain at constant viscosity. Dark slivers within the shear zones in Figs. 15b-e represent those parts of the shear zones which have undergone a change in deformation regime to GSS creep. Densely stippled areas indicate predominantly cohesionless brittle failure and frictional sliding. Normally stippled areas are cohesive frictional behavior (cataclasis). Headings of each rheological section indicate the relative time and upper crustal geothermal gradient during rifting. RE- and SI-transitions to GSS creep are described in the text (Section 5.4).

sensitivities of the mineral(s) governing viscous creep in the three lithological domains. In Fig. 15a, ductile fault zones (hatched regions) initially

occur in rocks with an arbitrarily chosen shear strength of 1 MPa or less. The initial rheological trajectory followed in these zones corresponds to the isothermal, constant strain-rate part of the grainsize-reduction path  $A-A_1$  in Fig. 8b. The extent to which ductile faulting also affects the tops of the relatively competent units will depend on the strength contrast of the two units at the temperature and strain-rate conditions of the deformation.

Grainsize reduction at the transition from brittle to crystal-plasticity (type (2) location above and in Fig. 15a) generally occurs at relatively low temperatures, low pressures and high stresses. Under these conditions, shear zones can nucleate at the base of the beak in Fig. 15a and may even involve a transition from either cataclasis or GSI creep to GSS creep (path  $B-B_1$  in Fig. 8b or path  $E-E_1$  in Fig. 9). Faulting above this level entails brittle failure and frictional sliding.

The localization of strain at reactions  $R_{x_1}$  and  $R_{x_2}$  in Fig. 15a can occur in granitic crustal segments of UC and LC if the strain rate is sufficiently high and the reaction kinetics are fast compared to the initial strain rate in the deforming rock. Should the reaction involve a hydrous phase, then the rocks on either side of the reactions may contain different amounts of structurally bound water or water-related species in nominally anhydrous minerals such as quartz or olivine. Since most such reactions require water (when formulated as retrograde reactions), the nominally anhydrous minerals on the lower temperature side of the reaction are depleted in water with respect to those on the higher temperature side. This can cause a relative decrease in creep strength on the higher temperature side of the reaction due to the weakening effect of water incorporated into a rheologically dominant (i.e. weak) mineral such as quartz, feldspar or olivine (see schematic inset beneath Fig. 15a; Griggs, 1967; Ord and Hobbs, 1986). Laboratory studies show that this effect is more likely to occur for initially small grain sizes (Chopra and Paterson, 1981; Jaoul et al., 1984). Alternatively, the rocks at type (3) locations may contain metastable mineral parageneses that are relicts of conditions

quite different from the ones prevailing at the onset of the most recent deformation. Orogenic terrains abound with examples of this sort, since intermediate and deep crustal rocks are exhumed during one orogenic event only to be reformed under upper crustal conditions, buried, and metamorphosed again during the next. Syn-tectonic reaction can lead to a breakdown of these minerals which can in turn favor a change in the deformation mechanism in the manner already referred to in Section 4.3 (paths  $C-D$  or  $E-F$  in Figs. 11 and 12a). Due to the cyclical, positive-feedback nature of deformational and metamorphic interactions, reactions such as this can accelerate the process of strain localization.

### 5.3. The rheology at time $t$

At time  $t_1$  during crustal thinning, the geotherm has increased to a maximum transient value, above the initial steady-state value,  $G_{ss}$  (Figs. 14 and 15b). The rocks which initially were at  $X_0$  and  $Y_0$  in the lithospheric section now occupy shallower levels at lower temperatures and pressures (points  $X_1$  and  $Y_1$  in Figs. 14 and 15b). The isostasy of the lithosphere during thinning causes the fault zones in the intermediate to lower crust and upper mantle to migrate passively upward with respect to their former positions. Due to the heightened geothermal gradient, brittle behavior is suppressed somewhat (i.e. viscous creep operates at shallower depths). Reactions such as  $R_{x_1}$  and  $R_{x_2}$  also occur at higher crustal levels for a given bulk composition, fluid composition and partial pressure. It is important to see that cooling during uplift produces increases in flow stress and shear viscosity for rocks deforming at a given strain rate (eqns. 1 and A8 in the Appendix). This is evident in Fig. 14 from the oblique angle between the  $P-T-t$  paths of points  $X$  and  $Y$ , and the essentially isothermal flow stress-viscosity contours in the GSI creep fields for quartzite and dunite. Thus, GSI creep in the retrograde ductile shear zones at  $X$  and  $Y$  involves grainsize reduction along the equilibrium piezometric plane in Fig. 8b. This equilibrium viscosity-grainsize relationship is

derived from eqns. (1) and (13) and can be expressed as:

$$\log d = \frac{1}{P} \left[ \log K - \frac{1}{n-1} \log \left( \frac{1}{\eta A \exp(-Q/RT)} \right) \right] \quad (15)$$

where the variables and constants are as defined in eqns. (1) and (13) or in the Appendix. Ductile shear at  $X_1$  and  $Y_1$  in Fig. 15b is concentrated into narrower zones than in Fig. 15a and has a lower viscosity than that of the adjacent, less deformed rocks (Section 4.5). Strain rates in the shear zones deforming at constant viscosity are estimated by assuming that stress within the shear zones is at the same levels as without. For these conditions, the minimum shear strain rate of the dry quartz-rich tectonite at  $X_1$  in Fig. 16b is therefore:

$$\dot{\gamma} = \frac{5 \text{ MPa}}{10^{14} \text{ MPa s}} = 5 \times 10^{-13} \text{ s}^{-1} \quad (16)$$

or five times higher than the regional strain rate of  $10^{-14} \text{ s}^{-1}$  outside of the shear zone. Of course, higher values of local shear strain rate result if the shear zones have higher stresses or a lower viscosity. Conversely, lower strain rates are obtained for a given flow stress if the viscosity of the shear zone increases.

#### 5.4. The rheology from times $t_2$ to $t_3$ : localized changes in creep regimes

At time  $t_2$ , the transient geothermal gradient has decreased to  $36^\circ\text{C}/\text{km}$  from its maximum value at  $t_1$  and the deforming rocks previously at  $X_1$  and  $Y_1$  are at yet lower temperatures and pressures corresponding to  $X_2$  and  $Y_2$  along their respective  $P$ - $T$ - $t$  trajectories (Figs. 14 and 15c). Shear stresses and/or strain rates in these shear zones have increased even more markedly. The estimated shear strain rate of shear zone  $X$  at  $t_2$  has risen to ca.  $5 \times 10^{-12} \text{ s}^{-1}$ , an order of magnitude higher than at  $t_1$ . For a shear zone at the litho-rheological boundary between LC and UM (at point  $Y_2$ ), a switch in deformation regimes from GSI to GSS creep and concomitant drop in viscosity may occur in two separate ways:

(1) When at  $t_2$  the  $P$ - $T$ - $t$  trajectory of the deforming rock intersects the discontinuous reaction curve,  $R_{x_1}$ , a drastic decrease in grainsize occurs and GSS creep (inferred to be diffusion-accommodated grain-boundary sliding) becomes the predominant mode of deformation. The rheological trajectory followed is that of path  $ABEF$  in Fig. 11. Since the reaction in Fig. 14 only affects rocks of LC bulk-composition, the reaction-enhanced softening is in this instance restricted to that part of the shear zone which affects LC rocks (see inset beneath Fig 15c). This type of reaction-enhanced transition from GSI to GSS creep was described in the previous section (e.g. Figs. 11 and 12) and is here called an *RE-transition* (reaction-enhanced), adapted from the original term for the process coined by White and Knipe (1978).

(2) If the shear stresses are sufficiently high (e.g. at high strain rates and low homologous temperatures), then the grainsize in the weakest mineral controlling the rheology of the rock will eventually become so small as to facilitate a switch to GSS creep (see discussion, Section 4.4). This type of transition is termed an *SI transition* (stress-induced) and is depicted with path  $A-A_1$  in Fig. 8b. SI transitions are favored at high stresses and will occur preferentially in more competent rocks initially undergoing GSI creep in a shear zone. For the ductile shear zone between LC and UM at points  $Y$  in Fig. 15, SI transitions will tend to occur within the cap of the relatively competent, olivine-rich UM rock (see lower right-hand inset, beneath Fig. 15e). As mentioned in Section 4.1, microstructures suggestive of GSS creep in nature are generally observed in mylonites with a grainsize of  $5$ – $15 \mu\text{m}$  or less. The ambient temperatures at which such fine, steady-state grainsizes are attained can be estimated with eqn. (15). These are plotted for different shear zone viscosities in Fig. 16, using the GSI power law for wet dunite derived in Section 1.2 and the Mercier et al. (1977) dynamically recrystallized grainsize piezometer for wet dunite. In a shear zone with a constant viscosity of  $10^{14} \text{ MPa s}$  assumed in Fig. 15, the transition to GSS creep in the UM rock is predicted to occur at about  $650^\circ\text{C}$ . This corresponds to time  $t_3$  along the  $P$ - $T$ - $t$  trajectory for

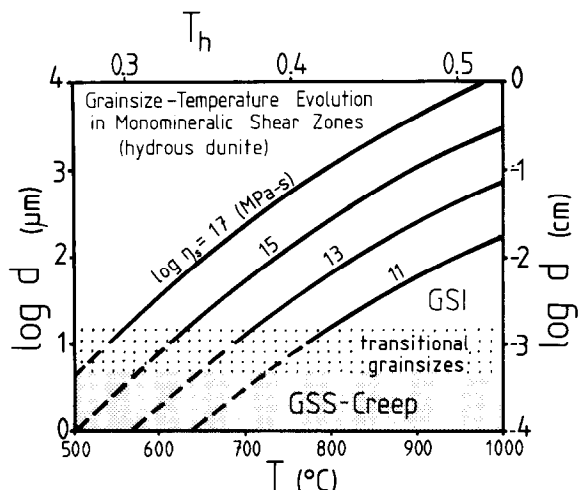


Fig. 16. Steady-state dynamically recrystallized grainsize versus temperature for various effective shear viscosities in the grainsize-insensitive (GSI) power law creep regime (eqn. 15). The piezometric relationship describing the equilibrium curves is no longer valid at grain sizes which are sufficiently small for grainsize-insensitive (GSS) power law creep (dashed parts of the viscosity contours). A transitional grain size of ca. 5 to 15  $\mu\text{m}$  (coarsely stippled region) is taken from microstructural and textural observations in mylonites (see Section 4.1). The stress-induced transition to GSS creep in polycrystalline olivine is predicted to occur at ca. 650  $^{\circ}\text{C}$  for a shear zone viscosity of  $10^{14}$  MPa s in Fig. 15d. Note that the use of this diagram assumes that: (1) dynamically recrystallized grain size has equilibrated with flow stress; (2) the shear zone is active over similar lengths of time as for changes in the ambient temperature in the lithosphere.

$Y$  in Figs. 14 and 15d. The predicted transitional temperature varies strongly with viscosity as well as with the piezometers and flow laws used. However, the value is in fair agreement with the predicted temperature range (600–700  $^{\circ}\text{C}$ ) for the GSI–GSS transition occurring at grain sizes of 10 to 50  $\mu\text{m}$  and comparable viscosities in the  $T$ – $\log d$  diagrams of Figs. 7a and b. It also corroborates microstructural observations suggesting that GSS creep in fine-grained olivine-rich rocks ( $d < 10 \mu\text{m}$ ) occurs under upper amphibolite to granulite facies conditions (Rutter and Brodie, 1988).

There are as yet no reported observations of large-scale SI transitions in nature. However, the essentially biminerally “SP mylonites” of Boullier and Gueguen (1975) may be interpreted as micro-scale examples of an SI transition; the minerals in such mylonites are small-scale analogues of the different lithologies in crustal scale shear zones.

Initially, the bulk of the strain in these mylonites was absorbed in the softer matrix mineral (olivine and feldspar in their figs. 1 and 6). Stress concentration in the more competent and slowly deforming clasts (pyroxene and amphibole in their figs. 1, 6 and 7) eventually resulted in dynamic recrystallization of the initially harder minerals to a grain size smaller than in the softer matrix. It is these initially “hard” minerals which display microstructural characteristics that are suggestive of GSS creep, indicating that grain size reduction of the more competent mineral leads to a strength inversion with respect to the initially softer matrix, at least on the thin-section scale.

Stress-induced transitions to GSS creep will probably only occur over a limited range of strength contrasts across litho-rheological boundaries. If the weakest mineral controlling GSI creep in the less competent lithology is significantly weaker than the weakest mineral controlling GSI creep in the more competent lithology, then almost all of the strain is accommodated in the less competent tectonite. Conversely, if the strength contrast between the two weakest minerals of the respective lithologies is small, then the critically high flow stresses necessary to induce an SI transition to GSS creep in either lithology may never accrue. Strain is accommodated more homogeneously and both lithologies continue to deform in the GSI-creep regime. Thus, SI transitions are very sensitive to compositional effects on the amplification of flow strength in addition to the temperature and strain-rate dependencies cited here and in Section 4.2. Moreover, SI transitions are easily pre-empted by weakening due to RE transitions. This not only explains the apparent ubiquity of RE transitions in nature, but also why RE transitions are expected to play a more important role during strain localization in the lithosphere.

#### 5.5. The rheology at time $t_4$ : progressive embrittlement

Continued deformation beyond time  $t_3$  in the model section considered here results in further crustal uplift and continued decrease in the transient geothermal gradient as the extending litho-

spheric section cools. At  $t_4$ , the  $P$ - $T$ - $t$  path of the shear zone separating UC and LC intersects the reaction curve  $R_{x_2}$  (Fig. 14), possibly resulting in an RE transition to GSS creep (Fig. 15e). The originally 47 km thick crustal section has been thinned to only 17 km. Eventually, effective pressures will reduce to levels which promote brittle failure and frictional sliding in shear zones where viscous creep was previously the predominant deformation regime. Embrittlement affects those shear zones first which have risen to very shallow depths (i.e. low effective pressures), are deforming at high strain rates, and which contain a high proportion of competent minerals (e.g. the olivine-rich part of the shear zone at  $Y_4$  in Fig. 15e).

### 5.6. Implications and limitations of the model

The evolutionary model presented here serves as a convenient means of showing the tectonic and thermal environments in which various rheological trajectories in fault zones can occur. In accordance with existing rheological models of the crust and upper mantle (e.g. Sibson, 1983; White and Bretan, 1985; Kuznir and Park, 1986; Meissner, 1986), large zones of detachment and shear are predicted to form at major litho-rheological boundaries. However, the litho-rheological stratification resulting from these models is strictly valid for initial increments of strain at the onset of orogeny or lithospheric stretching. The model in this paper demonstrates simply that accounting for the effects of evolving pressure, temperature and grain-size can lead to a far more complex simulation of lithospheric rheology. A subtle yet important feature of the model is that viscosity contrasts between compositionally different parts of the lithosphere are predicted to change with time and strain. At the outset (Fig. 15a), the viscosity-ratio across both litho-rheological boundaries (UC-LC and LC-UM) is predicted to be ca. 10 at the regional shear strain rate of  $10^{-14} \text{ s}^{-1}$ . By times  $t_3$  or  $t_4$  (Figs. 15d and e), the viscosity ratio across the UC-LC boundary is only 1 to 2, while that across the LC-UM boundary has increased to about 100. Such changes in the relative viscosity among large-scale lithological domains implies that

the level at which large strains are accommodated can shift on the scale of the lithosphere. In the model at hand, the deformational front migrates downwards, with much of the strain ultimately taken up in the large fault zone,  $Y$ , at the LC-UM interface. Clearly, the direction of migration and the magnitude of the viscosity contrasts depend strongly on the relative creep characteristics of the different lithological domains. The use of dry quartzite to simulate the rheology of the lower crust is done in the absence of reliable experimental flow laws for basic and feldspathic rocks. This probably leads to a significant underestimation of lower crustal strength.

The configuration of the strength and viscosity versus depth profiles in Fig. 15 partly reflects the twin assumptions of a constant regional strain rate and a constant viscosity history for the shear zones. In nature, stress and strain rate (and therefore also viscosity) can vary over several orders of magnitude, particularly in the vicinity of shear zones. Moreover, the viscosity in shear zones will vary with time. Changes in viscosity are due not only to temperature and strain-rate variations, as in this model, but are also related to stress amplification, a function of strain, crustal thickness, geothermal gradient and crustal composition (Kuznir and Park, 1986). Partial melting can also induce a considerable reduction in strength if the melt/rock ratio is high enough ( $> 30$ - $35 \text{ vol.}\%$ ) and the melt forms an interconnective network within the rock (Van der Molen and Paterson, 1979).

Syntectonic reaction-induced changes in rheology are more common than might be inferred from the two discontinuous reaction curves in Fig. 14. Rocks of different bulk composition have different domains of mineral stability. Tectonites developed within these various rock types will therefore cross syntectonic reaction curves at various times and places. More specifically, the locations at which reaction-induced or -enhanced strain localization occur depend on: (1) the bulk compositional profile of the lithospheric section; (2) the pressure (depth) and temperature stabilities of the different mineral facies in each compositional domain; (3) the kinetics of the metamorphic reactions with respect to the regional and local strain

rate; (4) the variations in effective pressure with depth and time; (5) the variations in the geothermal gradient with time and strain.

Taken together, the observations above suggest that two main environmental factors are responsible for the bewildering structural complexity in orogenic terrains: (1) the inherited compositional and structural heterogeneity, itself a product of the cumulative tectonometamorphic history prior to deformation; (2) the pressure–temperature–time path that various parts of the lithosphere follow during the most recent period of tectonism.

## 6. Summary and conclusions

Deformation of the lithosphere occurs under varying temperatures and effective pressures and involves different brittle and viscous creep regimes. The level at which strain localization occurs, the subsequent rheological evolution of high-strain shear zones, and ultimately the structure of the lithosphere all reflect the different dependencies of such deformation regimes on the imposed environmental conditions of temperature, pore and lithostatic pressures, stress, strain rate and rock-specific characteristics such as grainsize and mineralogy. The effect of variations in these parameters on the stability fields or equilibrium topologies of deformation regimes is illustrated with two- and three-dimensional deformation-regime diagrams that employ strain rate, temperature, pressure and grainsize coordinates.

The strain rate–temperature–pressure diagrams and strain-rate–temperature–grainsize diagrams in this paper show that the mechanical topologies of deformation regimes constructed from the extrapolation of experimental constitutive equations for polycrystalline olivine are in general agreement with the conditions and mechanisms of deformation in natural tectonites inferred from microstructural studies: low lithostatic pressures, high pore pressures and high strain rates promote brittle failure. Grainsize insensitive (GSI) power law creep predominates at most geologically relevant strain rates, stresses and temperatures in the crust and uppermost mantle. However, sufficiently small grain sizes and high temperatures favor grainsize sensitive (GSS) creep, particularly at lower strain

rates and stresses. Exponential law creep is restricted to a very narrow range of high stresses and strain rates near the transition between crystal plasticity and brittle behavior. The predictive value of such diagrams remains semiquantitative in view of the large experimental uncertainties, the present scarcity of data on the grainsize sensitivity of creep, the lack of a comprehensive theoretical basis for understanding brittle behavior, and finally, the poorly understood effects of time and strain.

Strain-rate–temperature–grainsize diagrams contoured for stress and viscosity are used in conjunction with experimentally calibrated paleopiezometers to constrain the rheological history of deformed rocks. This forms the basis for an evolutionary model of lithospheric rheology. The rheological evolution of a fault zone is related both to its location within a compositionally heterogeneous lithospheric section as well as to the pressure–temperature–time history of that section. First-order detachments are expected to nucleate at boundaries between major lithological–mineralogical domains in the lithosphere. Second-order detachments potentially occur at depths corresponding to changes in mineral stability and/or to the onset of partial melting. Progressive localization of strain at such zones of rheological instability occurs when the rate of strain hardening outside of the zones is greater than within the zones. If the subsequent shear zone activity is comparable to the periods over which changes in the ambient geotherm occur, then temperature influences the hardening rate and hence also the rate of strain localization. Strain localization is accelerated if grain sizes in the shear zone are sufficiently small and temperatures sufficiently high to allow the operation of GSS creep involving diffusion-accommodated granular flow. Such a transition in creep regimes from GSI to GSS creep can occur in two basic ways: (1) In rocks with a rheology governed by the GSI creep of one mineral, grainsize reduction leading to GSS creep is favored by the high flow stresses prevailing in low temperature and/or retrograde environments. (2) For most polymineralic rocks in both prograde and retrograde settings, a change to GSS creep is facilitated when there is a syntectonic reaction of

relatively competent relict minerals to form new, fine grained and/or weak minerals. This will occur at depths corresponding to the intersection of a given pressure–temperature–time path for an active shear zone with a discontinuous reaction curve separating mineralogical stability fields in a given compositional system.

The diagrams presented in this paper have both heuristic value and practical application to the study of naturally deformed rocks. For example, textures, microstructures, syntectonic mineral stabilities, and radiometric ages from exhumed shear zones can be used together with these diagrams to track the rheological evolution of natural deformations. This permits a comparison of the structure and rheology of crystalline rocks in the field with existing geophysical models of the crust and upper mantle. Alternatively, the use of such diagrams can be inverted to provide better constraints on the position of equilibrium boundaries between deformation regimes and mechanisms in nature.

### Acknowledgements

This work originated during a 17-month stay in the Geology Department (Rock Deformation Lab) at Imperial College, London. I am grateful to the members of that department, especially to Ernie Rutter, Kate Brodie and Mike Coward, for their kindness and hospitality. Holger Stuenitz and Dave Prior shared open, probing discussions that inspired and modified a number of ideas presented here. I also thank Ernie Rutter for several helpful discussions on the interpretation and extrapolation of rock-mechanical data. The paper benefited substantially from the insightful comments of M.S. Paterson and M.F. Ashby, as well as from the constructive criticism of two patient reviewers, W. Janny and an anonymous reader. Finally, my appreciation to I. Blaser and E. Remund for retyping the manuscript. The support of the Swiss National Science Foundation in the form of a post-doctoral grant is acknowledged.

### Appendix

To obtain mechanical equilibrium curves for the  $P$ – $T$ ,  $\log \dot{\gamma}$ – $T$  and  $T$ – $\log d$  deformation re-

gime maps in this paper, eqns. (1), (2), and (8) in the text are solved simultaneously for constant stress and the resulting equations are manipulated to express the equilibrium temperature of the deformation regimes as a function of  $\dot{\gamma}$ ,  $P$ ,  $\lambda$ ,  $d$ . The equations for the mechanical equilibrium boundaries are:

$$T_{\circ C} = (Q_{PL}) \left( R \left\{ \ln \left[ \frac{\sqrt{3}^{n+1} A}{\dot{\gamma} d^m} \right] + n \ln \left[ \frac{a + P(1-\lambda)(b-1)}{2} \right] \right\} \right)^{-1} - 273 \quad (A1)$$

for equilibrium between frictional sliding and power law creep (note:  $m = 0$  for grainsize-insensitive creep);

$$T_{\circ C} = (Q_{EL}) \left( R \left\{ \frac{\sqrt{3}}{2} C [a + P(1-\lambda)(b-1)] - \ln \frac{\dot{\gamma}}{\sqrt{3} B} \right\} \right)^{-1} - 273 \quad (A2)$$

for equilibrium between frictional sliding and exponential law creep;

$$T_{\circ C} = \frac{\left( \frac{Q_{EL}}{\sqrt{3} C} - \frac{Q_{PL}}{n} \right)}{R \left\{ \frac{1}{n} \ln \left( \frac{\dot{\gamma} d^m}{\sqrt{3}^{n+1} A} \right) - \frac{1}{\sqrt{3} C} \ln \left( \frac{\dot{\gamma}}{\sqrt{3} B} \right) \right\}} - 273 \quad (A3)$$

for equilibrium between exponential law creep and power law creep, where the case of  $Q_{EL} \neq Q_{PL}$  pertains;

$$T_{\circ C} = \left( Q_{GSI} - \frac{n_{GSI}}{n_{GSS}} Q_{GSS} \right) \times \left( R \left\{ \frac{n_{GSI}}{n_{GSS}} \ln \left[ \frac{\dot{\gamma} d^m}{\sqrt{3}^{n+1} A_{GSS}} \right] + \ln \frac{\sqrt{3}^{n+1} A_{GSI}}{\dot{\gamma}} \right\} \right)^{-1} - 273 \quad (A4)$$

for equilibrium between grainsize-insensitive and grainsize-sensitive power law creep regimes.

These equations can also be used to construct  $\dot{\gamma}$ – $T$  diagrams. Mechanical equilibrium equations

for  $\log \dot{\gamma}$ - $P$ ,  $\log \dot{\gamma}$ - $\log d$ , and  $\log \dot{\gamma}$ - $\lambda$  diagrams (not shown in this paper) are obtained via a similar manipulation of eqns. (A1) to (A4) above to express  $\log \dot{\gamma}$  in terms of  $P$ ,  $T$ ,  $d$ , and  $\lambda$ .

The viscous creep fields are contoured for lines of constant shear stress and constant effective shear viscosity. For the former, the equation are:

$$T_{\circ C} = \frac{Q_{EL}}{R \left\{ \ln \frac{\sqrt{3} B}{\dot{\gamma}} + \sqrt{3} C \tau \right\}} - 273 \quad (A5)$$

for the exponential law creep field.

$$T_{\circ C} = \frac{Q_{PL}}{R \left\{ \frac{\sqrt{3}^{n+1} A \tau^n}{\dot{\gamma} d^m} \right\}} - 273 \quad (A6)$$

for the power law creep field;

The equilibrium temperature for the effective shear viscosity contours (at a given shear strain rate) is:

$$T_{\circ C} = \frac{Q_{EL}}{R \left\{ \ln \sqrt{3} B + \sqrt{3} C \dot{\gamma} - \frac{1}{\eta} \right\}} - 273 \quad (A7)$$

for the exponential law creep field;

$$T_{\circ C} = \frac{Q_{PL}}{R \left\{ \ln \frac{\sqrt{3}^{n+1} A \dot{\gamma}^{n-1} \eta^n}{d^m} \right\}} - 273 \quad (A8)$$

for the power law creep field.

Note that if viscosity is expressed in Poise (P) units ( $\text{dyn s cm}^{-2}$ ), the  $\eta$ -term in eqns. (A7) and (A8) must be multiplied by  $10^{-9}$  kbar s  $P^{-1}$  (for  $A$  expressed in  $\text{kbar}^{-n} \text{s}^{-1}$ ) or by  $10^{-7}$  MPa s  $P^{-1}$  (for  $A$  expressed in  $\text{MPa}^{-n} \text{s}^{-1}$ ).

The brittle, frictional field is contoured for critical shear strength at failure by inverting eqn. (8) in the text:

$$P = \frac{2\tau - a}{(1 - \lambda)(b - 1)} \quad (A9)$$

#### Viscous creep parameters

- $A, B$  pre-exponential structure-functions for power law and exponential law creep, respectively;  
 $C$  stress function for exponential law creep;  
 $n$  creep exponent of power law creep;

- $n_{GSI}$  creep exponent of grainsize-insensitive (GSI) power law creep;  
 $n_{GSS}$  creep exponent of grainsize-sensitive (GSS) power law creep;  
 $Q$  activation energy for creep;  
 $Q_{EL}$  activation energy for exponential law creep;  
 $Q_{PL}$  activation energy for power law creep;  
 $Q_{GSI}$  activation energy for a grainsize-insensitive power law;  
 $Q_{GSS}$  activation energy for a grainsize-sensitive power law;  
 $m$  exponent of grainsize sensitivity ( $m = 0$  for GSI-creep);  
 $R$  universal gas constant;  
 $T$  absolute temperature (K);  
 $\dot{\gamma}$  octahedral shear strain rate ( $\text{s}^{-1}$ );  
 $\tau$  differential octahedral shear stress;  
 $\eta$  effective octahedral shear viscosity;  
 $\sqrt{3}$  shear factor (see eqns. 3 and 4).

#### Brittle-frictional parameters

- $a$  critical strength term in eqn. 8 of the text;  
 $b$  frictional coefficient term in eqn. 8 of the text;  
 $P$  total or lithostatic pressure;  
 $\lambda$  pressure ratio =  $P_{\text{pore}}/P$ .

#### References

- Ashby, M.F., 1972. A first report on deformation mechanism maps. *Acta Metall.*, 20: 887-897.  
 Ashby, M.F. and Verrall, R.A., 1978. Micromechanisms of flow and fracture, and their relevance to the rheology of the upper mantle. In: A. Kelly, A.H. Cook and G.W. Greenwood (Editors), *Creep of Engineering Materials and of the Earth*. *Philos. Trans. R. Soc. London, Ser. A*, 288: 59-95.  
 Atkinson, B.K., 1984. Subcritical crack growth in geological materials. *J. Geophys. Res.*, 89: 4298-4312.  
 Behrman, J.H., 1985. Crystal plasticity and superplasticity in quartzite; a natural example. *Tectonophysics*, 115: 101-129.  
 Borch, R.S. and Green, H.W., 1987. Dependence of creep in olivine on homologous temperature and its implications for flow in the mantle. *Nature*, 330: 345-348.  
 Bouillier, A.M. and Gueguen, Y., 1975. SP-mylonites: origin of some mylonites by superplastic flow. *Contrib. Mineral. Petrol.*, 50: 93-104.  
 Brodie, K., 1980. Variations in mineral chemistry across a

- phlogopite peridotite shear zone. *J. Struct. Geol.*, 2: 265–272.
- Brodie, K. and Rutter, E.H., 1985. On the relationship between deformation and metamorphism with special reference to the behavior of basic rocks. In: A.B. Thompson and D. Rubie (Editors), *Kinetics, Textures and Deformation*. *Adv. Phys. Geochem.*, Vol. 4. Springer, Berlin, pp. 138–179.
- Byerlee, J., 1978. Friction of rocks. *Pure Appl. Geophys.*, 116: 615–626.
- Carter, N.L. and Kirby, S.H., 1978. Transient creep and semi-brittle behavior of crystalline rocks. *Pure Appl. Geophys.*, 116: 807–839.
- Carter, N.L. and Tsenn, M.C., 1987. Flow properties of continental lithosphere. *Tectonophysics*, 136: 27–63.
- Chapman, D.S., 1986. Thermal gradients in the continental crust. In: J.B. Dawson et al. (Editors), *The Nature of the Lower Continental Crust*. *Spec. Publ., Geol. Soc. London*, 24: 63–70.
- Chopra, P.N. and Paterson, M.S., 1981. The experimental deformation of dunite. *Tectonophysics*, 42: 75–110.
- Dietrich, J.H., 1978. Time-dependent friction and the mechanics of stick-slip. *Pure Appl. Geophys.*, 116: 790–796.
- Donath, F.A., 1964. Strength variation and deformational behavior in anisotropic rock. In: W.R. Judd (Editor), *State of Stress in the Earth's Crust*. Elsevier, Amsterdam, pp. 281–297.
- Donath, F.A. and Fruth, L.S., 1971. Dependence of strain-rate effects on deformation mechanism and rock-type. *J. Geol.* 79: 347–371.
- Donath, F.A., Faill, R.T. and Tobin, D.G., 1971. Deformation mode fields in experimentally deformed rock. *Geol. Soc. Am. Bull.*, 82: 1441–1462.
- Etheridge, M.A. and Wilkie, J.C., 1979. Grainsize reduction, grain boundary sliding and the flow strength of mylonites. *Tectonophysics*, 58: 159–178.
- Freeman, B. and Ferguson, C., 1986. Deformation mechanism maps and micromechanisms of rocks with distributed grain sizes. *J. Geophys. Res.*, 91: 3849–3860.
- Garofalo, F., 1965. *Fundamentals of Creep and Creep-Rupture in Metals*. Macmillan, New York, N.Y., 258 pp.
- Green, H.W. and Hobbs, B.E., 1984. Pressure dependence of creep in dry polycrystalline olivine (abstr.). *Eos, Trans. Am. Geophys. Union*, 65: 1107.
- Griggs, D., 1967. Hydrolytic weakening of quartz and other silicates. *Geophys. J.R. Astron. Soc.*, 14: 19–31.
- Handy, M.R., 1986. The structure and rheological evolution of the Pogallo Fault Zone, a deep crustal dislocation in the Southern Alps of Northwestern Italy. Ph.D. Thesis, Univ. of Basel, 327 pp.
- Heitzmann, P., 1987. Calcite mylonites in the Central Alpine “root zone”. *Tectonophysics*, 135: 207–215.
- Hurford, A.J., 1986. Cooling and uplift patterns in the Lepontine Alps and an age of movement of the Insubric Fault Line, South-Central Switzerland. *Contrib. Mineral. Petrol.*, 92: 413–429.
- Jaoul, O., Tullis, J. and Kronenberg, A., 1984. The effect of varying water content on the behavior of Heavittree quartzite. *J. Geophys. Res.*, 89: 4298–4312.
- Jordan, P., 1987. The deformational behavior of biminerale limestone–halite aggregates. *Tectonophysics*, 135: 185–197.
- Karato, S.I. and Ogawa, M., 1982. High pressure recovery of olivine: implications for creep mechanisms and creep activation volume. *Phys. Earth Planet. Inter.*, 28: 102–117.
- Karato, S.I., Paterson, M.S. and Fitzgerald, J.D., 1986. Rheology of synthetic olivine aggregates: effect of grain size and of water. *J. Geophys. Res.*, 89: 4298–4312.
- Kekulawala, K.R.S.S., Paterson, M.S. and Boland, J.N., 1981. An experimental study of the role of water on quartz deformation. In: N.L. Carter et al. (Editors), *Mechanical Behavior of Crustal Rocks*. *Geophys. Monogr., Am. Geophys. Union*, 24: 49–60.
- Kruhl, J.H. and Voll, G., 1978–1979. Deformation and metamorphism of the Western Finero Complex. *Mem. Sci. Geol.*, 33: 95–109.
- Kumazawa, M. and Anderson, O.L., 1969. Elastic moduli, pressure derivatives, and temperature derivatives of single-crystal olivine and single-crystal forsterite. *J. Geophys. Res.*, 74: 5961–5972.
- Kuznir, N.J. and Park, R.G., 1986. Continental lithosphere strength: the critical role of lower crustal deformation. In: J.B. Dawson et al. (Editors), *The Nature of the Lower Continental Crust*. *Spec. Publ., Geol. Soc. London*, 24: 79–93.
- Lachenbruch, A.H., Sass, J.H. and Galanis, S.P., 1985. Heat flow in southernmost California and the origin of the Salton Trough. *J. Geophys. Res.*, 90: 6709–6736.
- Meissner, R., 1986. Twenty years of deep seismic reflection profiling in Germany—a contribution to our knowledge of the nature of the lower Variscan crust. In: J.B. Dawson et al. (Editors), *The Nature of the Lower Continental Crust*. *Spec. Publ., Geol. Soc. London*, 24: 1–10.
- Mercier, J.-C.C., Anderson, D.A. and Carter, N.L., 1977. Stress in the lithosphere: inferences from steady state flow of rocks. *Pure Appl. Geophys.*, 115: 199–226.
- Mogi, K., 1974. On the pressure-dependence of the strength of rocks and the Coulomb fracture criterion. *Tectonophysics*, 21: 273–285.
- Mohammed, F.A. and Langdon, T.G., 1974. Deformation mechanism maps based on grain size. *Metall. Trans.*, 5: 2339–2345.
- Nishikawa, M., Kono, S. and Armaki, S., 1970. Melting of Lherzolite from Ichinomegata at High Pressures. *Phys. Earth Planet. Inter.*, 4: 138–144.
- Nye, J.F., 1953. The flow law of ice from measurements in glacier tunnels, laboratory experiments and the Jungfrau borehole experiment. *Proc. R. Soc. London*, 219: 477–489.
- Ord, A. and Hobbs, B.E., 1986. Experimental control of the water-weakening effect in quartz. In: B.E. Hobbs and H.C. Heard (Editors), *Mineral and Rock Deformation: Laboratory Studies*. *Geophys. Monogr., Am. Geophys. Union*, 36: 51–72.
- Paterson, M.S., 1987. Problems in the extrapolation of laboratory rheological data. *Tectonophysics*, 133: 33–43.
- Poirier, J.P. and Liebermann, R.C., 1984. On the activation volume for creep and its variation with depth in the Earth's lower mantle. *Phys. Earth Planet. Inter.*, 34: 77–84.

- Post, R.L., 1977. High-temperature creep of Mt. Burnet Dunite. *Tectonophysics*, 42: 75–110.
- Price, N.J., 1975. Rates of deformation. *J. Geol. Soc.*, 131: 553–575.
- Ramsay, J.G., 1980. Shear zone geometry: a review. *J. Struct. Geol.*, 2: 83–99.
- Ross, J.V., Avé Lallement, H.G. and Carter, N.L., 1979. Activation volume for creep in the upper mantle. *Science*, 203: 261–263.
- Ross, J.V., Avé Lallement, H.G. and Carter, N.L., 1980. Stress-dependence of recrystallized grain- and subgrain size in olivine. *Tectonophysics*, 70: 39–61.
- Rubie, D.C., 1983. Reaction enhanced ductility; the role of solid–solid univariant reactions in the deformation of the crust and mantle. *Tectonophysics*, 96: 331–352.
- Rutter, E.H., 1972. The influence of interstitial water on the rheological behavior of calcite rocks. *Tectonophysics*, 14: 13–33.
- Rutter, E.H., 1976. The kinetics of rock deformation by pressure-solution. *Philos. Trans. R. Soc. London, Ser. A*, 283: 203–219.
- Rutter, E.H. and Brodie, K., 1987. The role of transiently fine-grained reaction products in syntectonic metamorphism: natural and experimental examples. *Can. J. Earth Sci.*, 24: 556–564.
- Rutter, E.H. and Brodie, K., 1988. The role of tectonic grain size reduction in the rheological stratification of the lithosphere. *Geol. Rundsch.*, 77: 295–308.
- Rutter, E.H. and Mainprice, D.H., 1978. The effect of water on stress-relaxation of faulted and unfaulted sandstone. *Pure Appl. Geophys.*, 116: 634–654.
- Schmid, S.M., 1975. The Glarus overthrust: field evidence and mechanical model. *Eclogae Geol. Helv.*, 68: 247–280.
- Schmid, S.M., 1982. Microfabric studies as indicators of deformation mechanisms and flow laws operative in Mountain Building. In: K.J. Hsü (Editor), *Mountain Building Processes*. Academic Press, London, pp. 95–110.
- Schmid, S.M., Boland, J.N. and Paterson, M.S., 1977. Superplastic flow in fine grained limestone. *Tectonophysics*, 43: 257–291.
- Schmid, S.M., Zingg, A. and Handy, M.R., 1987. The kinematics of movements along the Insubric Line and the emplacement of the Ivrea Zone. *Tectonophysics*, 135: 47–66.
- Schwenn, M.B. and Goetze, C., 1978. Creep of olivine during hot-pressing. *Tectonophysics*, 48: 41–60.
- Shelton, G., Tullis, J. and Tullis, T., 1981. Experimental high temperature and high pressure faults. *Geophys. Res. Lett.*, 8: 55–58.
- Shimada, M., Cho, A. and Yukatake, H., 1983. Fracture strength of dry silicate rocks at high confining pressures and the activity of acoustic emission. *Tectonophysics*, 96: 159–172.
- Shimamoto, T. and Logan, J.M., 1981a. Effects of simulated clay gouges on the sliding behavior of Tennessee Sandstone. *Tectonophysics*, 75: 243–255.
- Shimamoto, T. and Logan, J.M., 1981b. Effects of simulated nonclay gouges on the sliding behavior of Tennessee Sandstone. *J. Geophys. Res.*, 89: 4298–4312.
- Sibson, R.H., 1977. Fault rocks and fault mechanisms. *J. Geol. Soc.*, 133: 191–213.
- Sibson, R.H., 1983. Continental fault structure and the shallow earthquake source. *J. Geol. Soc.*, 140: 741–767.
- Steck, A. and Tièche, J.C., 1976. Carte géologique de l'anti-forme peridotitique de Finero avec des observations sur les phases de déformation et de recristallisation. *Schweiz. Mineral. Petrogr. Mitt.*, 56: 501–512.
- Stel, H., 1986. The effect of cyclic operation of brittle and ductile deformation on the metamorphic assemblage in cataclases and mylonites. *Pure Appl. Geophys.*, 124: 289–307.
- Stesky, R.M., 1978. Rock-friction effect of confining pressure, temperature, and pore pressure. *Pure Appl. Geophys.*, 116: 690–704.
- Stesky, R.M., Brace, W.F., Riley, D.K. and Robin, P.-Y.F., 1974. Friction in faulted rock at high temperature and pressure. *Tectonophysics*, 23: 177–203.
- Stocker, R.L. and Ashby, M.F., 1973. On the rheology of the upper mantle. *Rev. Geophys. Space Phys.*, 11: 391–426.
- Tsenn, M.C. and Carter, N.L., 1987. Upper limits of power law creep of rocks. *Tectonophysics*, 136: 1–26.
- Turner, F.J., 1981. *Metamorphic Petrology; Mineralogical, Field and Tectonic Aspects*. McGraw-Hill, New York, N.Y., 2nd edn., 524 pp.
- Twiss, R.D., 1976. Structural superplastic creep and linear viscosity in the earth's mantle. *Earth Planet. Sci. Lett.*, 33: 86–100.
- Twiss, R.D., 1977. Theory and applicability of a recrystallized grainsize paleopiezometer. In: M. Wyss (Editor), *Stress in the Earth*. *Pure Appl. Geophys.*, 115: 227–244.
- Van der Molen, I. and Paterson, M.S., 1979. Experimental deformation of partially-melted granite. *Contrib. Mineral. Petrol.*, 70: 299–318.
- Vogt, P., 1962. *Geologisch-petrographische Untersuchungen im Peridotitstock von Finero*. *Schweiz. Mineral. Petrogr. Mitt.*, 42: 59–125.
- Watterson, J., 1975. Mechanism for the persistence of tectonic lineaments. *Nature (London), Phys. Sci.*, 244: 276–278.
- Weertman, J., 1968. Dislocation climb theory of steady state creep. *Am. Soc. Metals Trans.*, 61: 681–694.
- Weertman, J., 1970. The creep strength of the earth's mantle. *Rev. Geophys. Space Phys.*, 8: 145–168.
- White, S.H., 1976. The effects of strain on the microstructures, fabrics, and deformation mechanisms in quartzites. *Philos. Trans. R. Soc. London, Ser. A*, 283: 69–86.
- White, S.H., 1977. Geological significance of recovery and recrystallization processes in quartz. *Tectonophysics*, 39: 143–170.
- White, S.H. and Bretan, P.G., 1985. Rheological controls on the geometry of deep faults and the tectonic delamination of the continental crust. *Tectonics*, 4: 303–310.
- White, S.H. and Knipe, R.J., 1978. Transformation- and reac-

- tion-enhanced ductility in rocks. *J. Geol. Soc. London*, 135: 513–516.
- White, S.H., Drury, M.R., Ion, S.E. and Humphreys, F.J., 1985. Large strain deformation studies using polycrystalline magnesium as a rock-analogue. Part I: grain size paleopiezometry in mylonite zones. *Phys. Earth Planet. Inter.*, 40: 201–207.
- Wojtal, S. and Mitra, G., 1986. Strain Hardening and Softening in Fault Zones. *Geol. Soc. Am. Bull.*, 97: 674–687.
- Zingg, A., 1983. The Ivrea and Strona–Ceneri zones (Southern Alps, Ticino and N-Italy)—a review. *Schweiz. Mineral. Petrogr. Mitt.*, 63: 361–392.
- Zobach, M.D., Prescott, W.H. and Kreuger, S.W., 1985. Evidence for lower crustal strain-localization in southern New York. *Nature*, 317: 705–707.